

# Reconstructing magma degassing and fragmentation: The 1060 CE Plinian eruption of Medicine Lake Volcano, California

Thomas Giachetti<sup>a,\*</sup>, Helge M. Gonnermann<sup>b</sup>, Joshua A. Crozier<sup>b</sup>

<sup>a</sup>*Department of Geological Sciences, University of Oregon, Eugene, OR, USA.*

<sup>b</sup>*Department of Earth Science, Rice University, Houston, TX, USA.*

---

## Abstract

We assess whether permeable open-system degassing significantly affects sustained explosive eruptions of silicic magma. The Plinian phase of the 1060 CE Glass Mountain eruption of Medicine Lake Volcano, California, was used as a test case. Analysis of porosity and permeability of Glass Mountain pyroclasts, together with numerical model of eruptive magma ascent and degassing, indicates that the effect of open-system degassing is negligible. The divergence of the permeable gas flux results in a small decrease in the pressure of exsolved magmatic vapor within bubbles. However, this pressure decrease is negligible compared to the closed-system case. The main control on magma fragmentation, which is considered the defining mechanism for explosive eruptions of silicic magma, is the ratio of the characteristic viscous time scale for bubble growth to the characteristic decompression time. This ratio defines a Péclet number,  $Pe_\eta$ . For values of  $Pe_\eta \gtrsim 1$  the GM magma is predicted to have fragmented, because pressure inside the growing bubbles cannot decrease as fast as the surrounding pressure. The characteristic time scale of permeable gas flow, divided by the characteristic decompression time, defines a second Péclet number,  $Pe_k$ . Under all conditions  $Pe_k \gg 1$  for the Plinian phase of the Glass Mountain eruption, indicating that permeable open-system degassing had a negligible effect on

---

\*Corresponding author

*Email address:* `tgiachet@uoregon.edu` (Thomas Giachetti)

the buildup of pressure inside bubbles. However, once the magma fragmented into pyroclast size pieces, open-system degassing should have rapidly dissipated any excess pressure inside bubbles. Consequently, the porosity of pyroclasts is thought to be representative of magma vesicularity at the time of fragmentation. Assuming, therefore, that the measured range in sample porosities reflects the range of conditions at which the erupting magma fragmented, it is possible to constrain the eruption model using the measured porosities. The ensuing model results indicate that fluctuations in eruption rate would have resulted in changes in the fragmentation depth of the order of hundreds of meters. At any given time, however, fragmentation is predicted to have occurred over a depth interval of a few tens of meters only.

*Keywords:* Plinian eruption, open-system degassing, percolation modeling, permeability, diffusion modeling, fragmentation

---

## 1. Introduction

Volcanic eruptions are driven by the degassing of magma during its final ascent to the surface (Sparks, 1978; Jaupart and Allègre, 1991; Woods and Koyaguchi, 1994; Gonnermann and Manga, 2007). Bubbles of supercritical fluid, mainly water, nucleate and grow during magma ascent because volatile solubility decreases (Toramaru, 1990; Papale, 1999; Liu et al., 2005; Zhang et al., 2007). In silicic magma melt, once water has exsolved to within about one weight percent or less, viscosity becomes sufficiently large to adversely affect the rate of bubble growth. As a consequence the pressure inside bubbles decreases at a slower rate than the surrounding pressure (Lensky et al., 2001; Gonnermann and Manga, 2007). This leads to bubble overpressure, potentially to the point of exceeding the magma's tensile strength, in which case the magma fragments (McBirney and Murase, 1970; Sparks, 1978; Alidibirov, 1994; Dingwell, 1996; Zhang, 1999; Spieler et al., 2004; Mueller et al., 2008; Gonnermann, 2015).

During sustained explosive eruptions fragmentation releases the magmatic vapor and the fragmented magma can expand rapidly into a dilute gas-pyroclast

17 mixture of low viscosity (Fowler et al., 2010), as schematically illustrated in  
18 Figure 1. Unless the magma fragments down to the size of individual bub-  
19 bles, the magma must be permeable in order for the vapor to escape from the  
20 interior of the individual fragments (Rust and Cashman, 2011). The process  
21 of permeable open-system degassing, also referred to as permeable outgassing,  
22 has received considerable discussion within the context of both non-fragmented  
23 effusively erupting magma and explosively erupting magma (e.g. Eichelberger  
24 et al., 1986; Westrich and Eichelberger, 1994; Sparks, 2003; Rust and Cashman,  
25 2004; Burgisser and Gardner, 2005; Okumura et al., 2006; Wright et al., 2009;  
26 Rust and Cashman, 2011; Degruyter et al., 2012; Nguyen et al., 2014).

27 Permeability is thought to be a consequence of bubble coalescence. As bub-  
28 bles grow, they impinge upon one another and inter-bubble melt films thin to  
29 the point of rupture (e.g. Toramaru, 1988; Proussevitch et al., 1993a; Castro  
30 et al., 2012a; Nguyen et al., 2013). As inter-bubble melt films rupture, adja-  
31 cent bubbles become interconnected. Silicate melt viscosity allows the coalesced  
32 bubbles to form a network of interconnected bubbles that persists on eruptive  
33 time scales and becomes preserved with the quenched pyroclasts. This inter-  
34 connected bubble network allows the vapor inside bubbles to move relative to  
35 the erupting magma at rates that are proportional to the local product of per-  
36 meability and gradient in gas pressure. Furthermore, permeability is thought  
37 to be a nonlinear function of the volume fraction of bubbles and equivalent to  
38 the permeability preserved in pumice (Taylor et al., 1983; Eichelberger et al.,  
39 1986; Westrich and Eichelberger, 1994; Klug and Cashman, 1996; Sparks, 2003;  
40 Takeuchi et al., 2008; Wright et al., 2009; Rust and Cashman, 2011).

41 Fragmentation of silicic magma is thought to be a consequence of bubble  
42 overpressure (e.g., McBirney and Murase, 1970; Alidibirov and Dingwell, 1996;  
43 Zhang, 1999; Ichihara et al., 2002; Spieler et al., 2004; Namiki and Manga, 2005;  
44 Gonnermann, 2015). If there is a divergence in the permeable gas flux, the re-  
45 sultant loss in vapor, relative to closed-system degassing, results in a decrease in  
46 pressure inside bubbles and has the potential to adversely affect brittle magma  
47 fragmentation (Mueller et al., 2008). Decompression-fragmentation experiments

48 have shown that during near instantaneous decompression of vesicular pyroclasts  
49 some fraction of the initial pressure within the vesicles dissipates due to per-  
50 meable gas flow as the fragmentation wave propagates into the sample (Fowler  
51 et al., 2010; McGuinness et al., 2012). If the permeability is high enough, this  
52 pressure loss must be compensated by an increase in initial pressure in order for  
53 the sample to fragment upon decompression (Mueller et al., 2008). Instead of  
54 the effect of permeable open-system degassing within the zone of fragmentation,  
55 here we assess to what extent permeable gas flow up to the fragmentation zone  
56 affects sustained explosive activity.

57 To this end we study the Plinian phase of the 1060 CE Glass Mountain  
58 (GM) eruption of Medicine Lake Volcano, California. The GM eruption was  
59 a relatively weak Plinian eruption and therefore potentially more susceptible  
60 to changes in gas pressure brought about by permeable open-system degassing,  
61 compared to explosive eruptions of higher intensity. Furthermore, the Plinian  
62 phase of the Glass Mountain eruption transitioned after a relatively small erup-  
63 tion volume from sustained explosive activity to effusive activity, and the Plinian  
64 fallout deposits are well-characterized and easily accessible (Section 2).

65 We have assessed the effect of permeable outgassing on the eruption through  
66 numerical modeling of eruptive magma ascent, including diffusive bubble growth  
67 with permeable open-system degassing (Section 5). In order to include per-  
68 meable gas flow in the modeling, we first measured pyroclast porosities and  
69 permeabilities (Section 3). We then used percolation modeling to estimate the  
70 percolation threshold and derive a functional dependence of permeability on  
71 porosity (Section 4). The latter is one of the dependent variables solved for by  
72 the model, whereas permeability is not. A discussion of our results is provided  
73 in Section 6.

## 74 **2. Geological context**

75 The GM eruption has been the last event of the post-glacial eruptive activity  
76 of Medicine Lake Volcano, California (Anderson, 1933; Heiken, 1978; Donnelly-

77 Nolan et al., 1990, 2008). The eruption consisted of a Plinian phase followed  
78 by the emplacement of rhyolite-dacite flows, with a total erupted volume of  
79 approximately 1 km<sup>3</sup> (Heiken, 1978). The Plinian phase produced a fallout  
80 deposit of 0.27 km<sup>3</sup> (Donnelly-Nolan et al., 2007), consisting of very poorly  
81 sorted rhyolitic lapilli with no evidence for deposition by pyroclastic flows. All  
82 pumices are texturally homogeneous, essentially phenocrysts free (<5% Heiken,  
83 1978), and with a microlite content of approximately 3 vol% (Stevenson et al.,  
84 1996). The chemical composition of the tephra is similar to that of the GM  
85 rhyolitic obsidian, and has a SiO<sub>2</sub> content of 72-75 wt% (Anderson, 1933; Heiken,  
86 1978; Grove and Donnelly-Nolan, 1986; Grove et al., 1997).

87 Magmatic inclusions and experimental petrologic studies indicate that the  
88 GM magma formed under near H<sub>2</sub>O-saturated conditions at pressures of 100-200  
89 MPa (Grove et al., 1997), equivalent to depths of 3-6 km, and initial magmatic  
90 water content of about 4-6 wt% (Liu et al., 2005). In agreement with these  
91 petrological and geochemical studies, seismic tomography has identified a silicic  
92 magma body of up to few tens of cubic kilometers at 3-7 km below the eastern  
93 part of Medicine Lake caldera (Evans and Zucca, 1988; Chiarabba et al., 1995;  
94 Donnelly-Nolan et al., 2008).

### 95 **3. Sample analysis**

#### 96 *3.1. Porosity measurement*

97 Twenty-four representative pumices from the Plinian phase of the GM erup-  
98 tion were collected across a wide stratigraphic range of the fallout deposit lo-  
99 cated near the northern margin of the GM rhyolitic flow. Samples vary from  
100 approximately 0.01 m to 0.30 m in size, are phenocryst free, and do not show  
101 any obvious gradient in porosity or bubble size from center to margin. One  
102 to three cores of 0.02 m in diameter were drilled from each pyroclast and then  
103 cut to produce 1-9 sub-samples of 0.01-0.02 m length, resulting in a total of 76  
104 sub-samples. Total porosity,  $\phi_t$  (refer to Table 1 for symbols), as well as con-  
105 nected porosity,  $\phi_c$ , were determined by He-pycnometry on each sub-sample,

106 using a density of the solid phase,  $\rho_m = 2,430 \text{ kg.m}^{-3}$  (Giachetti et al., 2015).  
 107 Sample porosity was determined by averaging the porosities obtained on the  
 108 1-9 sub-samples. The connected porosity, which is the volume fraction of in-  
 109 terconnected vesicles that are also connected to the exterior of the sample, is  
 110 used to constrain the percolation modeling by which we obtain the functional  
 111 dependence of sample permeability on porosity (Section 4).

### 112 *3.2. Permeability measurement*

113 The cylindrical sub-samples were mounted on plexiglas and sealed with high  
 114 viscosity epoxy along the radial perimeter so that air flow during permeability  
 115 measurements was in the axial direction. The volumetric flow rate of laboratory  
 116 air was measured at different inlet pressures using a capillary flow porometer.  
 117 The maximum applied pressure difference was 0.5 MPa, and the measured fluxes  
 118 varied from approximately  $10^{-4}$  to  $5 \text{ m.s}^{-1}$ . Because inertial effects can be sig-  
 119 nificant while measuring the permeability of volcanic rocks (Rust and Cashman,  
 120 2004; Takeuchi et al., 2008; Degruyter et al., 2012; Nguyen et al., 2014), we used  
 121 the Forchheimer’s equation for a compressible fluid,

$$122 \quad \frac{P_2^2 - P_1^2}{2P_1L} = \frac{\eta_g}{k}q + \frac{\rho_g}{k_2}q^2, \quad (1)$$

123 to recover the permeability of each sample (Appendix A). Here  $P_2$  and  $P_1$  are  
 124 the inlet and outlet pressures, respectively,  $q$  is the volume flux of air,  $L$  is the  
 125 length of the sample,  $\eta_g$  and  $\rho_g$  are respectively the viscosity and density of the  
 126 air,  $k$  is the Darcian permeability, and  $k_2$  is the inertial (non-Darcian) perme-  
 127 ability. The minimum measurable volumetric flow rate was  $8 \times 10^{-9} \text{ m}^3.\text{s}^{-1}$ . For  
 128 a cylindrical sample of 0.02 m in length and 0.01 m in radius, the average size  
 129 of our samples, the minimum measurable permeability was  $\sim 10^{-17} \text{ m}^2$ . This  
 130 is about three orders of magnitude lower than the minimum permeability mea-  
 131 sured for any sample. As for porosity, the sample permeability was determined  
 132 by averaging the permeabilities obtained for the individual sub-samples.

### 133 3.3. Measured porosities and permeabilities

134 Results of porosity and permeability analysis on the GM pumices are pro-  
135 vided in Figure 2 (red filled circles), together with data pertaining to other  
136 Plinian pumices from the literature (filled gray symbols). Values of  $\phi_t$  for the  
137 GM pyroclasts are typical for Plinian fallout and fall in the range 0.69-0.87.  
138 Values for  $\phi_c$  vary from 0.56 to 0.86 and are positively correlated with  $\phi_t$  (Fig-  
139 ure 2a). Values of  $k$  of all the GM pumices range between approximately  $10^{-14}$   
140 and  $10^{-11}$  m<sup>2</sup>, and are similar to permeabilities from other Plinian eruptions  
141 (Figure 2b). There is a broad power-law relationship between  $k$  and  $\phi_t$ , as usu-  
142 ally observed for Plinian clasts (Figure 2b; e.g. Klug and Cashman, 1996; Rust  
143 and Cashman, 2011; Nguyen et al., 2014). The functional relations between  $\phi_c$   
144 and  $\phi_t$ , as well as between  $k$  and  $\phi_t$  were both constrained using percolation  
145 modeling.

## 146 4. Percolation modeling

### 147 4.1. Background

148 Similar to other porous materials, the permeability of vesicular volcanic rocks  
149 can be assessed within the framework of percolation theory (e.g., Sahimi, 1994;  
150 Blower, 2001a), and a power-law can be used to describe the relationship be-  
151 tween Darcian permeability and total porosity

$$152 \quad k = b \times r^2 (\phi_t - \phi_{cr})^c, \quad (2)$$

153 where  $r$  is the average bubble radius, and  $b$ ,  $c$  and  $\phi_{cr}$  are fitting parameters.  $\phi_{cr}$   
154 is called the percolation threshold, which is defined as the porosity below which  
155 no interconnected pore space spans the entire sample and permits permeable  
156 flow. In general, values of  $b$ ,  $c$ , and  $\phi_{cr}$  have been difficult to constrain, in part  
157 because of the lack in samples with porosities close to  $\phi_{cr}$  (e.g., Mueller et al.,  
158 2005; Degruyter et al., 2010; Rust and Cashman, 2011; Nguyen et al., 2014).  
159 To overcome this obstacle we used a percolation model.

160 The percolation model is based on the assumption that the complex net-  
161 work of vesicles in a pumice can be reproduced by spheres that are randomly  
162 distributed in a volume. Where two spheres overlap they are assumed to be  
163 interconnected. At some threshold volume fraction of spheres, that is at  $\phi_{cr}$ ,  
164 enough spheres are interconnected to create a percolating cluster. The perco-  
165 lating cluster is a single cluster of interconnected spheres that spans the entire  
166 volume and would in principle allow fluid flow through the sample from one  
167 end to another. Here we used a percolation model wherein spheres drawn at  
168 random from a size distribution equal to that measured for GM samples (Ap-  
169 pendix B) were randomly placed in a cubic volume of  $10^{-8} \text{ m}^3$ . The overlap of  
170 spheres creates percolating clusters, and the flow resistance across these clusters  
171 depends on the size and number of apertures between individual bubbles. From  
172 this network of resistors permeability is calculated using the approach outlined  
173 by Blower (2001a,b) and detailed in Appendix C. Repeated realizations of the  
174 percolation model across a broad range of total porosities results in a functional  
175 relation between  $\phi_c$  and  $\phi_t$ , as well as  $k$  and  $\phi_t$ . For several cases permeability  
176 was calculated in three orthogonal directions and resultant permeabilities were  
177 always within 2% of one another.

178 For two spheres to be considered coalesced (interconnected), their centers  
179 need to be separated by a distance,  $d$ , less than  $(1 - \epsilon/2) \times (r_1 + r_2)$ , where  
180  $r_1$  and  $r_2$  are the radius of each sphere and  $0 \leq \epsilon \leq 1$  (Appendix C).  $\epsilon$  is  
181 a parameter that reduces the degree of connectivity for otherwise overlapping  
182 spheres. When applied to pumice,  $\epsilon$  accounts for the presence of deformed  
183 vesicles that are not coalesced. When modeled as spheres of equivalent radii  $r_1$   
184 and  $r_2$ , deformed bubbles would have a center to center distance of  $d < (r_1 + r_2)$ ,  
185 and would be considered as coalesced if  $\epsilon = 0$  (Figure C.1; Blower, 2001b). The  
186 significance and impact of  $\epsilon$  on the percolation-model results are discussed in  
187 Appendix C.

188 *4.2. Results*

189 Results of the percolation model show that a consistent functional relation-  
190 ship between  $\phi_c$  and  $\phi_t$  can be obtained (Appendix C), and the measured values  
191 of  $\phi_c$  vs.  $\phi_t$  can be reproduced using values of  $\epsilon$  in the range 0.2-0.6 (Figure 2a).  
192 At the same time the percolation modeling allows the estimation of  $k$  down to  
193 the percolation threshold (Figure 2b). Thus, it is possible to obtain a robust  
194 functional relation between  $k$  and  $\phi_t$  that can be used in the eruption model to  
195 calculate permeability and, hence, predict permeable open-system degassing.

196 **5. Eruption model**

197 *5.1. Conceptual model*

198 The eruption model is used to assess the effect of permeable open-system  
199 degassing on magma fragmentation and, hence, sustained explosive activity dur-  
200 ing the Plinian phase of the GM eruption. The eruption model encompasses a  
201 conduit flow model (Section 5.3), which predicts the change in magma pressure,  
202  $P_m$ , as a function of depth,  $z$ . The conduit flow model is coupled via  $P_m$  to a  
203 diffusive bubble growth model (Section 5.4). The bubble growth model consti-  
204 tutes solving the coupled equations for momentum balance of a growing bubble  
205 and the mass balance of H<sub>2</sub>O vapor inside the bubble. The latter includes a  
206 source term due to diffusion of H<sub>2</sub>O into the bubble and a sink term that repre-  
207 sents the difference between permeable flow of H<sub>2</sub>O into and out of the bubble.  
208 The source term is obtain from solving for the diffusion of H<sub>2</sub>O through the  
209 surrounding melt into the bubble. The sink term is obtained from solving for  
210 the vertical permeable flow of H<sub>2</sub>O vapor due to gradients in the pressure of  
211 H<sub>2</sub>O vapor inside bubbles, and uses the functional relation between  $k$  and  $\phi_t$   
212 obtained from the percolation modeling.

213 The combined model predicts bubble size,  $R$ , vesicle volume fraction,  $\phi_t$ ,  
214 pressure inside bubbles,  $P_g$ , and in the surrounding melt,  $P_m$ , all as a function  
215 of depth. The eruption model is constrained using predicted values of  $\phi_t$  and  
216  $R$ , which are required to match measured porosities for the GM pyroclasts

217 (Figure 2) as well as the average bubble radius ( $\sim 10 \mu\text{m}$ , see Appendix B).  
218 These values are assumed to be representative of the magma at the time of  
219 fragmentation, thereby allowing the assessment of how model parameters, in  
220 particular permeable open-system degassing, affect magma fragmentation.

## 221 5.2. Principal simplifying assumptions

### 222 5.2.1. Constant discharge rate and conduit radius

223 Based on field observations and grain-size data, Heiken (1978) determined  
224 that the  $0.27 \text{ km}^3$  of GM tephra were deposited during a Plinian phase as air-fall  
225 deposits. This phase lasted probably 3-6 hours as suggested by a comparison  
226 with other Plinian eruptions of similar magnitude (e.g., Carey and Sigurdsson,  
227 1989; Mastin et al., 2009). Because throughout the deposit GM pumices are  
228 remarkably homogeneous in their composition and morphology (Heiken, 1978),  
229 we surmise that the eruption conditions did not vary significantly for most of  
230 the duration of the eruption. We therefore assume steady and isothermal condi-  
231 tions on time scales over which magma traversed the conduit between chamber  
232 and vent ( $\sim 10$  minutes), an assumption commonly adopted while modeling sus-  
233 tained explosive eruptions (e.g., Wilson et al., 1980; Jaupart and Allègre, 1991;  
234 Dobran, 1992; Woods, 1995; Mastin and Ghiorso, 2000; Melnik, 2000; Papale,  
235 2001; Mastin, 2002; Slezin, 2003; Mitchell, 2005; Macedonio et al., 2005; Koy-  
236 aguchi, 2005; Gonnermann and Houghton, 2012; Colucci et al., 2014; Nguyen  
237 et al., 2014).

238 Specifically, this means that we use a constant mass discharge rate,  $Q$ , and  
239 a constant conduit radius,  $a$ , both of which are poorly constrained for the GM  
240 eruption. Conduit radii typically assumed or estimated for Plinian eruptions  
241 are 15-50 m (e.g., Carey and Sigurdsson, 1985; Dobran, 1992; Klug and Cash-  
242 man, 1996; Gerlach et al., 1996; Clarke et al., 2002; Hildreth and Fierstein,  
243 2012), while mass discharge rates during Plinian eruptions, inferred from lithic  
244 dispersal patterns, are usually within the range  $10^6$ - $10^9 \text{ kg}\cdot\text{s}^{-1}$  (e.g., Carey and  
245 Sigurdsson, 1989; Mastin et al., 2009). We therefore explored a range of values  
246 of  $Q$  and  $a$  to assess the sensitivity of the model results on these two parameters.

247 *5.2.2. Volatile content and initial pressure*

248 Giachetti et al. (2015) estimated that the amount of magmatic water dis-  
249 solved in the matrix-glass of the GM pyroclasts is 0.20-0.45 wt%, which is  
250 similar to the water content of the rhyolitic obsidian that was subsequently  
251 emplaced (e.g., Eichelberger and Westrich, 1981; DeGroat-Nelson et al., 2001;  
252 Castro et al., 2005). The GM magma therefore lost >90% of its magmatic water  
253 during eruptive ascent between magma chamber and quenching of the pyroclast.  
254 CO<sub>2</sub>, F, Cl and S together account for <3% of the total volatile content of the  
255 GM pyroclasts (Anderson, 1933; Eichelberger and Westrich, 1981). Whereas  
256 H<sub>2</sub>O remains mostly soluble at pre-eruptive storage depths, volatiles like CO<sub>2</sub>,  
257 if initially present in the magma, are expected to have been at considerably  
258 lower concentrations prior to eruption than H<sub>2</sub>O (e.g., Wallace, 2005; Papale,  
259 2005; Burton et al., 2013). We therefore only consider H<sub>2</sub>O in our modeling,  
260 an assumption that is justifiable, because CO<sub>2</sub> is not expected to significantly  
261 affect model results (Gonnermann and Houghton, 2012).

262 The magma was under near H<sub>2</sub>O-saturated conditions at initial pressures  
263 of 100-200 MPa (Grove and Donnelly-Nolan, 1986; Grove et al., 1997). Most  
264 model calculations were run for an initial pressure of 100 MPa, corresponding to  
265 an initial water saturation of 3.9 wt% (Liu et al., 2005), and an initial depth of  
266 approximately 3.9 km, assuming near-lithostatic pressure and an average rock  
267 density of 2,600 kg.m<sup>-3</sup>. The sensitivity of model results to this assumed initial  
268 pressure was evaluated and is discussed in Appendix D.1.

269 *5.2.3. Bubble size distribution*

270 We model the growth of a single representative spherical bubble (e.g., Prous-  
271 sevitch et al., 1993a; Lensky et al., 2004). Although the GM pyroclasts contain  
272 a distribution of vesicle sizes, our approach has the benefit of attaining a rigor-  
273 ous prediction of pressure within the growing bubble. To be representative of  
274 the majority of bubbles within the erupting magma, we used a bubble number  
275 density,  $N = 4 \times 10^{14}$  per m<sup>3</sup> of melt. This value was obtained by analyzing the  
276 bubble size distribution of a representative GM pumice with a total porosity of

277 0.75 (Appendix B). In order to assess the sensitivity of our choice in  $N$  on model  
 278 predictions we compared results for different values of  $N$  (Appendix D.2). We  
 279 find that, all else being the same, an increase in  $N$  leads to more rapid buildup  
 280 of pressure within bubbles and somewhat deeper fragmentation. For example, a  
 281 change in  $N$  by one order of magnitude leads to a change in the fragmentation  
 282 depth of approximately 50 m.

#### 283 5.2.4. Open-system degassing

284 We explicitly account for the fact that water vapor can flow independently  
 285 through interconnected bubbles within the erupting magma, once the value of  
 286  $\phi_t$  exceeds the percolation threshold. It has been hypothesized that permeable  
 287 gas flow may also occur at a scale larger than the bubble-scale, due to brittle  
 288 shear deformation of the magma (e.g., Jaupart and Allègre, 1991; Stasiuk et al.,  
 289 1996; Jaupart, 1998; Gonnermann and Manga, 2003; Tuffen et al., 2003; Tuffen  
 290 and Dingwell, 2005; Okumura et al., 2009; Cabrera et al., 2011; Castro et al.,  
 291 2012b, 2014). At present there are no robust quantitative estimates for the  
 292 magnitude of this effect and we do not attempt to account for such open-system  
 293 degassing in our model.

#### 294 5.3. Equations for magma flow

295 We assume one-dimensional, isothermal magma flow at a constant mass flow  
 296 rate within a cylindrical conduit of constant diameter, and solve the equations  
 297 of mass and momentum conservation (Wilson et al., 1980; Mastin, 2002)

$$298 \quad \frac{dQ}{dz} = \frac{d(\rho u \pi a^2)}{dz} = 0, \quad (3)$$

299 and

$$300 \quad \rho u \frac{du}{dz} = -\rho g - \rho u^2 \frac{f}{a} - \frac{dP_m}{dz}. \quad (4)$$

301 Equations (3) and (4) can be combined to give (Mastin and Ghiorso, 2000)

$$302 \quad -\frac{dP_m}{dz} = \frac{\rho g + \rho u^2 f/a}{1 - M^2}, \quad (5)$$

303 where it is assumed that the conduit is of constant size.  $z$  is vertical coordinate  
 304 and is directed upward.  $M$  denotes the Mach number,  $Q$  is the magma mass

305 discharge rate,  $u$  is the average magma velocity, and  $\rho = \rho_g \phi_t + \rho_m (1 - \phi_t)$  is the  
 306 magma density.  $\phi_t = (R/S)^3$  is the volume fraction of bubbles, where  $3\pi(S^3 -$   
 307  $R^3)/4$  is the constant bubble number density  $N$ , and  $S$  the half distance between  
 308 bubbles.  $a$  is the radius of the cylindrical conduit and assumed constant,  $g$  is  
 309 the acceleration due to gravity, and  $f$  is the friction factor given by (Wilson  
 310 et al., 1980; Dobran, 1992; Mastin and Ghiorso, 2000; Koyaguchi, 2005)

$$311 \quad f = \frac{16}{\text{Re}} + f_0 = \frac{8\eta}{\rho u a} + f_0. \quad (6)$$

312 Here  $f_0$  is assumed constant at 0.02 (Wilson et al., 1980; Mastin and Ghiorso,  
 313 2000),  $\eta$  is the magma viscosity, and Re is the Reynolds number. Similar to  
 314 previous work, we found that variations in  $f_0$  in the range 0.002-0.02 do not  
 315 significantly affect our model results (Mastin and Ghiorso, 2000). We used the  
 316 formulation of Pal (2003) to include the effect of bubbles on viscosity (see also  
 317 Gonnermann and Manga, 2007; Mader et al., 2013). To this end we calculated  
 318 the H<sub>2</sub>O-, temperature- and composition-dependent melt viscosity,  $\eta_m$ , using  
 319 the formulation of Hui and Zhang (2007). The composition of GM rhyolite was  
 320 taken from Heiken (1978), and we account for the variations in melt viscosity  
 321 associated with diffusion gradients in H<sub>2</sub>O concentrations using the effective  
 322 melt viscosity,  $\eta_e$ , derived by Lensky et al. (2001).

#### 323 *5.4. Equations for bubble growth*

324 Our model includes a sub-grid scale calculation of diffusive bubble growth, in  
 325 order to predict dissolved H<sub>2</sub>O, bubble size,  $R$ , volume fraction of bubbles,  $\phi_t$ ,  
 326 and pressure inside bubbles,  $P_g$ . The latter two are used to calculate permeable  
 327 gas flow (Section 5.5) as well as conditions for magma fragmentation (Section  
 328 5.6). The diffusive bubble growth calculation solves the coupled momentum and  
 329 mass balance equations for an idealized spherical bubble. The approach follows  
 330 established methods (Amon and Denson, 1984; Arefmanesh and Advani, 1991;  
 331 Proussevitch et al., 1993a), and is based on the simplifying assumptions that  
 332 all bubbles at a given depth are of the same size, distributed throughout the

333 magma in a uniform packing geometry, and at a bubble number density equal  
 334 to that determined from the GM samples (Appendix B).

335 Diffusive bubble growth is coupled to conduit flow via magma pressure,  $P_m$ ,  
 336 which is the dependent variable for conduit flow (Section 5.3), and the boundary  
 337 condition for bubble growth. Magma density and viscosity, which vary due to  
 338 bubble growth and a decrease in H<sub>2</sub>O content of the melt, respectively, are  
 339 required for the conduit flow calculations and provide further coupling between  
 340 conduit flow and bubble growth.

341 The momentum balance equation for a representative bubble, neglecting  
 342 inertial terms due to the large melt viscosity (Proussevitch et al., 1993a), is  
 343 given by

$$344 \quad P_g - P_m = \frac{2\gamma}{R} + \frac{4\eta_e}{R} \frac{dR}{dt}, \quad (7)$$

345 where  $\gamma$  is the surface tension of water in rhyolitic melt. The value of sur-  
 346 face tension for hydrated rhyolite varies with temperature, pressure and water  
 347 content, but because realistic variations in  $\gamma$  do not significantly affect bub-  
 348 ble growth (Gonnermann and Houghton, 2012), it was assumed constant at  
 349 0.06 N.m<sup>-1</sup> (Epel’baum et al., 1973), which is reasonable estimate for rhyolitic  
 350 magma (Hurwitz and Navon, 1994; Lyakhovsky et al., 1996; Bagdassarov et al.,  
 351 2000; Mangan and Sisson, 2000; Mourtada-Bonnefoi and Laporte, 2004; Hamada  
 352 et al., 2010; Gardner and Ketcham, 2011; Gonnermann and Gardner, 2013).

353 The conservation of water, given by Equation (8) states that the rate of  
 354 change in mass of water vapor inside the bubble equals the sum of two terms:

$$355 \quad \frac{d(\rho_g R^3)}{dt} = 3R^2 \rho_m D \left( \frac{\partial C}{\partial r} \right)_{r=R} + \frac{1}{N(1 - \phi_t)} \frac{\partial(q_k \rho_g)}{\partial z}. \quad (8)$$

356 The first term on the right hand side of Equation (8) denotes the integrated  
 357 flux of H<sub>2</sub>O across the melt-vapor interface, where the radial coordinate of the  
 358 melt-vapor interface defines the bubble radius  $r = R$ . The second term on the  
 359 right hand side of Equation (8) is the divergence of the permeable gas flow  
 360 through the bubble. Here  $t$  denotes time,  $\rho_g$  is the density of water inside  
 361 the bubble (Kerrick and Jacobs, 1981),  $\rho_m = 2,430 \text{ kg.m}^{-3}$  is the density of  
 362 the rhyolitic melt (Giachetti et al., 2015) and assumed constant, and  $C$  is the

363 spatially dependent water content in the melt.  $D$  is the diffusivity of water in  
 364 rhyolitic melt, which depends on  $P_m$ , temperature and  $C$  (Ni and Zhang, 2008).  
 365  $N$  is the bubble number density in the melt and is assumed constant (Appendix  
 366 B).  $q_k$  denotes the permeable gas flux (Section 5.5). The initial bubble radius  
 367 was taken as  $10^{-7}$  m, and model results do not significantly depend on the  
 368 choice of initial values for  $R$  (Appendix D.3).

369 The decrease in  $P_m$  during magma ascent will induce bubble growth (Equa-  
 370 tion (7)), which in turn causes  $P_g$  to decrease.  $H_2O$  solubility at the melt-vapor  
 371 interface depends on  $P_g$ , which tends to decrease as the bubble grows in size.  
 372 Consequently, there will be a decrease in  $H_2O$  concentrations toward the melt-  
 373 vapor interface, causing  $H_2O$  to diffuse toward the interface where it exsolves.  
 374 The diffusion of  $H_2O$  within the melt is calculated using

$$375 \quad \frac{\partial C}{\partial t} + \frac{dR}{dt} \frac{\partial C}{\partial r} = \frac{1}{r^2} \frac{\partial}{\partial r} \left( Dr^2 \frac{\partial C}{\partial r} \right), \quad (9)$$

376 where  $R \leq r \leq S$  is the radial coordinate for the melt surrounding the bubble.  
 377 Because  $R$  and  $S$  are functions of time, this equation is solved in a Lagrangian  
 378 frame of reference, using an implicit finite difference scheme with non-uniform  
 379 grid spacing (Proussevitch et al., 1993a). This facilitates adequate resolution  
 380 of the steep concentration gradients at the melt-vapor interface. The boundary  
 381 condition at  $r = S$  is given by

$$382 \quad \left( \frac{\partial C}{\partial r} \right)_{r=S} = 0, \quad (10)$$

383 and at  $r = R$  by

$$384 \quad (C)_{r=R} = C_{P_g}, \quad (11)$$

385 where  $C_{P_g}$  is the solubility of water in rhyolite at  $P_g$  (Liu et al., 2005).

### 386 5.5. Equations for permeable gas flow

387 We assume that from the depth where  $\phi_t \geq \phi_{cr}$  the exsolved  $H_2O$  vapor  
 388 flows through bubbles from high to low  $P_g$ . The divergence of this flux results  
 389 in permeable open-system degassing. Relative to closed-system bubble growth,  
 390 permeable open-system degassing may reduce  $\Delta P = P_g - P_m$  and, hence, the

391 rate of bubble growth as well as  $\phi_t$ . To calculate  $q_k$  we used Forchheimer's  
 392 equation

$$393 \quad \frac{\partial P_g}{\partial z} = \frac{\eta_g}{k} q_k + \frac{\rho_g}{k_2} q_k^2. \quad (12)$$

394 Here,  $\eta_g \approx 4.2 \times 10^{-5}$  Pa.s is the viscosity of the supercritical H<sub>2</sub>O vapor (gas)  
 395 calculated using a steam table (Haar et al., 1984), and  $k$  is the Darcian per-  
 396 meability. The latter was calculated using magma porosity and the empirical  
 397 formulation for  $k(\phi_t)$  obtained by fitting the measured GM data with the per-  
 398 colation model (Section 4.2, Appendix C).  $k_2$  is the inertial permeability and  
 399 was calculated using the relationship between the measured values of  $k$  and  $k_2$   
 400 (Appendix E).

401 The divergence of the permeable mass flux of H<sub>2</sub>O vapor was calculated it-  
 402 eratively using a predictor-corrector method, wherein conduit flow and diffusive  
 403 bubble growth are calculated repeatedly until calculated values of  $q_k$  between  
 404 subsequent iterations have converged. During the first iteration, denoted by  
 405  $i = 1$ , it is assumed that

$$406 \quad k^{i=1}(z) = k_2^{i=1}(z) = 0. \quad (13)$$

407 The resultant prediction of  $\phi_t^{i=1}(z)$  is then used to calculate  $\hat{k}^{i=1}(z)$ , and  $\hat{k}_2^{i=1}$   
 408 is obtained from the functional relation between  $k_1$  and  $k_2$  (Appendix E). At  
 409 subsequent iterations values of  $k$  are given by

$$410 \quad k^i(z) = \alpha k^{i-1}(z) + (1 - \alpha) \hat{k}^{i-1}(z), \quad (14)$$

411 where  $0 < \alpha < 1$ . For all calculations we found good convergence using  $\alpha =$   
 412  $9/10$ .

### 413 5.6. Condition for magma fragmentation

414 During ascent  $\eta$  increases by several orders of magnitude, predominantly due  
 415 to the exsolution of H<sub>2</sub>O. Once the viscous resistance of the surrounding melt  
 416 becomes sufficiently large to affect the rate of bubble growth,  $P_g$  decreases at a  
 417 slower rate than  $P_m$ . This results in a rapidly increasing overpressure  $\Delta P = P_g -$   
 418  $P_m$ . Experimentally it has been shown that upon rapid decompression vesicular

419 magma fragments at an overpressure greater than or equal to a threshold value  
420  $\Delta P_{\text{f}}$  that is inversely proportional to  $\phi_{\text{t}}$  (e.g., Alidibirov, 1994; Zhang, 1999;  
421 Spieler et al., 2004; Mueller et al., 2008).

422 To predict the conditions at which magma would fragment, we use the em-  
423 pirical fragmentation criterion of Mueller et al. (2008),

$$424 \quad \Delta P_{\text{f}} = \frac{(8.21 \times 10^5) \sqrt{k} + \sigma_{\text{m}}}{\phi_{\text{t}}}, \quad (15)$$

425 where  $\sigma_{\text{m}} = 1.54$  MPa is the effective tensile strength.

426 This formulation does not imply that permeability affects the tensile strength  
427 of magma. Rather, it accounts for the fact that during fragmentation experi-  
428 ments, where a porous sample is subjected to a near instantaneous decompres-  
429 sion, some fraction of the initial pressure within the sample’s vesicles dissipates  
430 by permeable gas flow when the fragmentation wave propagates through the  
431 sample (Fowler et al., 2010; McGuinness et al., 2012; Gonnermann, 2015). Al-  
432 though our modeling accounts for permeable gas flow below the fragmentation  
433 zone, it does not explicitly model the fragmentation process. Instead, we as-  
434 sume that the effect of permeable outgassing within the narrow fragmentation  
435 zone can be accounted for by the permeability-adjusted fragmentation pressure  
436 of Mueller et al. (2008), and using a jump condition in pressure across the  
437 fragmentation zone (e.g., Melnik et al., 2005).

## 438 6. Model results and discussion

439 In order to assess a wide range of feasible eruption scenarios, we explored  
440 200 combinations of mass discharge rate,  $Q$ , and conduit radius,  $a$ , to evaluate  
441 the effect of permeable open-system degassing on magma ascent and fragmen-  
442 tation. We will, however, first present results for what we consider as a *best*  
443 *case* model result, in order to illustrate the salient processes (Sections 6.1-6.2).  
444 Subsequently we will present and discuss the results of the parametric analysis,  
445 which will provide a broad assessment of feasible eruption scenarios (Section  
446 6.3).

447 *6.1. Best case: ascent to fragmentation*

448 The results of our best case model are summarized in Figure 3, and a dis-  
 449 cussion of why this model constitutes a *best case* is deferred until Section 6.3.  
 450 This model used a conduit radius of 24 m, a mass discharge rate of  $1.1 \times 10^7$   
 451  $\text{kg}\cdot\text{s}^{-1}$ , and an initial pressure of 100 MPa. The rate of decrease in  $P_m$  acceler-  
 452 ates noticeably, once the average water content of the melt approaches 1 wt.%.  
 453 At this point magma viscosity begins to exceed  $\sim 10^6$  Pa.s and viscous pressure  
 454 loss becomes large. At the same time  $\phi_t$  increases, as does the magma ascent  
 455 velocity. High viscosity also adversely affects the rate of bubble growth. Con-  
 456 sequently  $P_g$  does not keep pace with the decrease in  $P_m$ , resulting in a rapid  
 457 buildup of overpressure. Because the fragmentation threshold  $\Delta P_f$  is inversely  
 458 proportional to  $\phi_t$  (Equation (15)), values of  $\Delta P$  and  $\Delta P_f$  rapidly converge,  
 459 until magma fragmentation is predicted to occur. For the case shown in Figure  
 460 3 fragmentation is predicted at a depth of about 1 km.

461 To provide further insight into the conditions that lead to magma fragmen-  
 462 tation we define a Péclet number

$$463 \text{Pe}_\eta = \frac{\tau_\eta}{\tau_{\text{dec}}}, \quad (16)$$

464 where  $\tau_\eta$  is the characteristic viscous time scale for bubble growth, and  $\tau_{\text{dec}}$  the  
 465 characteristic decompression time scale. If  $\text{Pe}_\eta \gtrsim 1$ , then viscosity adversely  
 466 affects the rate of bubble growth and bubbles will become pressurized, poten-  
 467 tially leading to magma fragmentation (Lensky et al., 2004; Gonnermann and  
 468 Manga, 2007). We define the viscous time scale as

$$469 \tau_\eta \equiv \frac{\eta_m}{\Delta P_f}, \quad (17)$$

470 where  $\Delta P_f \sim 10^6$  Pa is the characteristic pressure scale.

471 The characteristic decompression time scale,  $\tau_{\text{dec}}$ , is based on the fact that  
 472 below the level of fragmentation permeability and the rate of permeable gas  
 473 flow are largest. It is therefore in this region that open-system degassing is  
 474 most relevant. An equation for the rate of magma decompression,  $\dot{P}_m$ , can be

475 obtained by substituting  $u = Q/(\rho\pi a^2)$  in Equation (5), and assuming that  
 476  $(1 - M^2) \sim 1$  below the level of fragmentation. The resultant equation is

$$477 \quad \dot{P}_m = u \frac{dP_m}{dz} = \frac{gQ}{\pi a^2} + \frac{8\eta Q^2}{\rho^2 \pi^2 a^6} + \frac{f_0 Q^3}{\rho^2 \pi^3 a^7}. \quad (18)$$

478 Because large magma viscosity is required for the buildup of overpressure,  
 479 magma flow below the fragmentation level is at Reynolds numbers of  $\sim 1$  or  
 480 less. Consequently, the decompression rate is dominated by the second term on  
 481 the right-hand-side of Equation (18), and scales as  $Q^2/a^6$ . We thus define

$$482 \quad \tau_{\text{dec}} \equiv \frac{\Delta P_f \rho^2 a^6}{\eta Q^2}, \quad (19)$$

483 using  $\Delta P_f \sim 10^6$  Pa as the characteristic pressure scale. The viscous Péclet  
 484 number is therefore given by

$$485 \quad \text{Pe}_\eta = \frac{\eta_m \eta Q^2}{\Delta P_f^2 \rho^2 a^6}. \quad (20)$$

486 For values of  $\eta_m \sim 10^7$  Pa.s and  $\rho \sim 10^3$  kg.m<sup>-3</sup> we find that  $\text{Pe}_\eta \sim 1$  for this  
 487 *best case*, indicating conditions at the threshold to the buildup of overpressure  
 488 and fragmentation.

## 489 6.2. Best case: open-system degassing

490 Figure 4 represents a magnification of the results from Figure 3 over the  
 491 depth range where magma is permeable. In addition, results for the open-system  
 492 model are compared to a closed-system model with the same initial conditions  
 493 and model parameters (Figure 4e). Permeable open-system degassing has a  
 494 negligible effect on model results, which can be understood in terms of the ratio  
 495 of the characteristic time scale for permeable open-system degassing,  $\tau_k$ , to the  
 496 characteristic decompression time scale,  $\tau_{\text{dec}}$ .

497 This ratio defines a second Péclet number

$$498 \quad \text{Pe}_k = \frac{\tau_k}{\tau_{\text{dec}}}. \quad (21)$$

499 If  $\text{Pe}_k \gg 1$ , then there is insufficient time for significant permeable open-system  
 500 degassing over eruptive time scales.

501 We define the characteristic permeable degassing time scale as

$$502 \quad \tau_k \equiv \max \left[ \frac{\eta_g L^2}{k \Delta P_f}, \sqrt{\frac{\rho_g L^3}{k_2 \Delta P_f}} \right], \quad (22)$$

503 where  $\Delta P_f \sim 10^6$  Pa is the characteristic pressure scale, and  $L \sim 100$  m the  
 504 corresponding length scale of permeable degassing, consistent with predictions  
 505 of the distance between the percolation threshold and magma fragmentation  
 506 (Figure 3c). This definition of  $\tau_k$  allows for the possibility that permeable gas  
 507 flow is at either small or large Forchheimer number (Degruyter et al., 2012).  
 508 For the range in values of  $k$  and  $k_2$  estimated for the GM samples we find that

$$509 \quad \frac{\eta_g L^2}{k \Delta P_f} \gtrsim \sqrt{\frac{\rho_g L^3}{k_2 \Delta P_f}} \quad (23)$$

510 and, hence,

$$511 \quad \tau_k \equiv \frac{\eta_g L^2}{k \Delta P_f}. \quad (24)$$

512 The resultant Péclet number is given by

$$513 \quad \text{Pe}_k \sim \frac{\eta_g L^2 \eta Q^2}{k \Delta P_f^2 \rho^2 a^6}. \quad (25)$$

514 Using a conservatively large value of  $k \sim 10^{-10}$  m<sup>2</sup> (Appendix A), together  
 515 with  $\eta_g \sim 10^{-5}$  Pa.s, we find that  $\text{Pe}_k \gtrsim 10^3$ , confirming that permeable open-  
 516 system degassing should indeed be negligible.

517 For open-system degassing to significantly affect eruption conditions the  
 518 value of  $\text{Pe}_k$  must be reduced by about 3 orders of magnitude. A correspond-  
 519 ing increase in  $k$  is unlikely, at least if open-system degassing is solely due to  
 520 bubble-scale permeable gas flow. Instead, either other mechanisms for open-  
 521 system degassing must be dominant (Stasiuk et al., 1996; Gonnermann and  
 522 Manga, 2003; Tuffen et al., 2003; Cabrera et al., 2011; Castro et al., 2012b)  
 523 and/or a significant reduction in  $Q^2/a^6$  are required. However, as shown in  
 524 Section 6.3, a reduction in  $Q^2/a^6$  by itself will result in a transition to effusive  
 525 behavior before open-system degassing becomes effective. We therefore sug-  
 526 gest that it was not open-system degassing through networks of interconnected

527 bubbles which affected the transition from explosive to effusive activity at GM.  
 528 Rather it may have been due to a reduction in magma ascent rate, perhaps  
 529 because of a reduction in magma chamber pressure, or a change in the conduit  
 530 size.

### 531 6.3. The role of $Pe_\eta$

532 Figure 5a shows predicted values of  $\phi_t$  and  $\Delta P$  over a wide range in model  
 533 parameters  $Q$  and  $a$ . Also shown are the measured values of  $\phi_t$  for the GM  
 534 samples, as well as the resultant estimates of  $\Delta P_f$ , using the relationship between  
 535  $k$  and  $\phi_t$  and Equation (15). Furthermore, shown in gray is the range in  $\Delta P_f$   
 536 for porosity-permeability relations obtained from percolation modeling for the  
 537 range  $0.2 \leq \epsilon \leq 0.6$ . Given that the measured values of  $\phi_t$  in GM samples  
 538 probably represent magmatic conditions at the time of fragmentation (Section  
 539 6.5), our assessment of model predictions is based on a normalized root-mean-  
 540 square error, defined as

$$541 \quad \chi = \frac{1}{n} \sqrt{\sum_{i=1}^n \left[ \frac{(\Delta P(\phi_{t,i}) - \Delta P_{f,i})}{\Delta P_{f,i}} \right]^2}. \quad (26)$$

542 Here  $n = 24$  is the number of GM samples, and  $0 \leq \chi \leq 1$ .  $\Delta P(\phi_{t,i})$  is the  
 543 predicted overpressure at the value of  $\phi_t$  equal to the porosity of the  $i$ th GM  
 544 sample. Furthermore,  $\Delta P_{f,i}$  is the estimated value of fragmentation pressure  
 545 for the  $i$ th GM sample calculated using Equation (15) for the measured values  
 546  $\phi_{t,i}$  and  $k_i$ .

547 Values of  $\chi$ , for the range of models with different values of  $a$  and  $Q$ , are  
 548 shown as a function of  $Pe_\eta$  in Figure 5b. Only cases for which the magma  
 549 fragments between a depth of 2.5 km and the Earth's surface are shown.  $\chi$   
 550 reaches a minimum at  $Pe_\eta \approx 6$ , which is the case shown in Figures 3 and  
 551 4. As expected, the depth of fragmentation increases approximately with  $Pe_\eta$ .  
 552 At  $Pe_\eta \lesssim 0.8$  the magma reaches the Earth's surface before fragmentation is  
 553 predicted to occur. For  $Pe_\eta \gtrsim 60$  the porosity at fragmentation does not reach  
 554 the lowest measured value of GM samples.

555 *6.4. Fragmentation depth*

556 Figure 5c shows two illustrative cases, one of which being the case with the  
557 smallest value of  $\chi$  (solid blue curve,  $\text{Pe}_\eta \approx 6$ ). For this case fragmentation is  
558 predicted to occur between -1,070 m (if  $\epsilon = 0.6$ ) and -1,050 m (if  $\epsilon = 0.2$ ). Figure  
559 5b shows that reasonable fits to the GM data can be achieved with  $3 \lesssim \text{Pe}_\eta \lesssim 9$ ,  
560 which corresponds to a relatively wide range of fragmentation depths, between  
561 about -1.5 km and the Earth's surface (Figure 5a). The range in porosities  
562 and permeabilities observed in the GM pyroclasts suite may therefore record  
563 different times of the Plinian phase of the eruption, suggesting variations in  
564 mass discharge rate and conduit radius (hence, variations in  $\text{Pe}_\eta$ ), leading to  
565 fluctuations in the fragmentation depth. Whether there exists a progressive  
566 variation of the expected depth of fragmentation with time would require a  
567 more systematic sampling throughout the Plinian tephra deposit.

568 *6.5. Permeable outgassing after fragmentation*

569 At fragmentation, water diffusivity in the melt is  $D \sim 10^{-12} \text{ m}^2.\text{s}^{-1}$ , while  
570 the thickness of the melt shell is  $(S - R) \sim 10^{-6} \text{ m}$ , making the time scale for  
571 water diffusion  $\tau_{\text{dif}} \sim (S - R)^2/D \sim 1 \text{ s}$ . At fragmentation, the permeability  
572 of GM samples is  $k \gtrsim 10^{-14} \text{ m}^2$ , the viscosity of the gas  $\eta_g \sim 10^{-5} \text{ Pa.s}$ , and  
573 the pressure gradient  $\Delta P \sim 10^6 \text{ Pa}$ , leading to a characteristic time scale for  
574 permeable outgassing of  $\tau_k \lesssim 0.1 \text{ s}$  for a clast of size  $L \sim 10^{-2} \text{ m}$ . Because  
575  $\tau_k \ll \tau_{\text{dif}}$ , any water exsolved from the melt after fragmentation can readily  
576 be lost from the vesicular pyroclast and excess pressure inside bubbles will be  
577 rapidly dissipated.

578 The time scale for pyroclast expansion,  $\tau_{\text{exp}} \sim \eta_e/\Delta P$  is  $\sim 10 \text{ s}$ , given that  
579  $\eta_e \sim 10^7 \text{ Pa.s}$  at fragmentation. Therefore,  $\tau_k \ll \tau_{\text{exp}}$  and gas escape domi-  
580 nates over expansion. Consequently, significant post-fragmentation changes in  
581 porosity are unlikely, and supported by the absence of any obvious gradients  
582 in porosity or bubble size between center and margin of GM pumices (Heiken,  
583 1978).

584 Giachetti et al. (2015) showed that the magmatic water content of GM  
585 pumices is 0.2-0.5 wt%. The predicted water content at fragmentation of ap-  
586 proximately 1.1-1.3 wt% therefore suggests that GM pyroclasts lost approxi-  
587 mately 0.6-1.1 wt% of water after fragmentation by open-system degassing, and  
588 without significant change in pyroclast texture.

## 589 7. Conclusions

590 We presented results from combined textural analysis of pyroclasts and per-  
591 colation modeling, as well as modeling of open-system degassing during the 1060  
592 CE Plinian phase of the eruption of Medicine Lake Volcano, California. The  
593 eruption model shows that open-system degassing by vertical flow of magmatic  
594 vapor through the permeable magma was negligible and did not significantly  
595 impact fragmentation.

596 Sensitivity analysis of our model to conduit radius and mass discharge rate  
597 suggests that permeable outgassing cannot account for the transition from ex-  
598 plosive to effusive activity during the Glass Mountain eruption. It is possible  
599 that radial permeable outgassing through conduit walls and/or through perva-  
600 sive fractures, neither of which were modeled here, significantly affected magma  
601 fragmentation. However, there are no compelling observations to substantiate  
602 this. Rather, we believe that the transition from explosive to effusive activ-  
603 ity was caused by a decrease of the mass discharge rate or/and an increase in  
604 conduit size.

605 We find that the porosities and permeabilities measured in Glass Mountain  
606 pyroclasts are closely matched by models with a mass discharge rate of  $\sim 10^7$   
607  $\text{kg}\cdot\text{s}^{-1}$  and a conduit radius of about 25 m, resulting in magma fragmentation  
608 around 1 km below the Earth's surface. The decompression rate at fragmenta-  
609 tion is predicted at  $\sim 10^6 \text{ Pa}\cdot\text{s}^{-1}$  and corresponds to a melt viscosity of  $\sim 10^7$   
610  $\text{Pa}\cdot\text{s}$  and a water content in the melt of approximately 1 wt.%. A relatively wide  
611 range of fragmentation depths, between about -1.5 km and the Earth's surface,  
612 provide reasonable fits to the Glass Mountain samples. This may suggest that

613 collected pyroclasts represent different times of the Plinian phase, illustrating  
614 variations in mass discharge rate and/or conduit size, and hence, fluctuations  
615 in fragmentation depth.

616 For the measured pyroclast permeabilities, open-system degassing of pyro-  
617 clasts was rapid, and probably prevented significant post-fragmentation changes  
618 in porosity and permeability. Last but not least, we surmise that magma per-  
619 meability, instead of hindering the ability of magma to erupt explosively, may  
620 be a necessary condition to efficiently release gas from confining bubbles and  
621 enable the growth of incipient fractures, once the magma begins to fragment.

## 622 **8. Acknowledgments**

623 This material is based upon work supported by the National Science Foun-  
624 dation under grants EAR-1348072, EAR-1250451, and CMMI-1015069. Any  
625 opinions, findings, and conclusions or recommendations expressed in this ma-  
626 terial are those of the authors and do not necessarily reflect the views of the  
627 National Science Foundation.

## 628 **References**

- 629 Adams, N., Houghton, B., Fagents, S., Hildreth, W., 2006. The transition  
630 from explosive to effusive eruptive regime: The example of the 1912 No-  
631 varupta eruption, Alaska. *Geol. Soc. Amer. Bull.* 118, 620–634. doi:10.1007/  
632 s00445-006-0067-4.
- 633 Alidibirov, M., 1994. A model for viscous magma fragmentation during volcanic  
634 blasts. *Bull. Volcanol.* 56, 459–465. doi:10.1007/BF00302827.
- 635 Alidibirov, M., Dingwell, D.B., 1996. Magma fragmentation by rapid decom-  
636 pression. *Nature* 380, 146–148. doi:10.1038/380146a0.
- 637 Amon, M., Denson, C.D., 1984. A study of the dynamics of foam growth:  
638 analysis of the growth of closely spaced spherical bubbles. *Poly. Eng. Sci.* 24,  
639 1026–1034. doi:10.1002/pen.760241306.

- 640 Anderson, C.A., 1933. Volcanic history of Glass Mountain, northern California.  
641 Am. Jour. Sci. 5(26), 485–506. doi:10.2475/ajs.s5-26.155.485.
- 642 Anderson, C.A., 1941. Volcanoes of the Medicine Lake Highland, California.  
643 Univ. Calif. Berkeley Publ., Geol. Sci. 23, 215–276.
- 644 Arefmanesh, A., Advani, S., 1991. Diffusion-induced growth of a gas bubble in  
645 a viscoelastic fluid. Rheol. Acta 30, 274–283. doi:10.1007/BF00366641.
- 646 Bagdassarov, N.S., Dorfman, A., Dingwell, D.B., 2000. Effect of alkalis, phos-  
647 phorus, and water on the surface tension of haplogranite melt. Am. Mineral.  
648 85, 33–40.
- 649 Blower, J.D., 2001a. A three-dimensional network model of permeabil-  
650 ity in vesicular material. Comput. Geosci. 27, 115–119. doi:10.1016/  
651 S0098-3004(00)00066-2.
- 652 Blower, J.D., 2001b. Factors controlling permeability - porosity relationships in  
653 magma. Bull. Volcanol. 63, 497–504. doi:10.1007/s004450100172.
- 654 Burgisser, A., Gardner, J., 2005. Experimental constraints on degassing and  
655 permeability in volcanic conduit flow. Bull. Volcanol. 67, 42–56. doi:10.  
656 1007/s00445-004-0359-5.
- 657 Burton, M.R., Sawyer, G.M., Granieri, D., 2013. Deep carbon emissions from  
658 volcanoes. Rev. Mineral. Geochem 75, 323–354. doi:10.2138/rmg.2013.75.  
659 11.
- 660 Cabrera, A., Weinberg, R.F., Wright, H.M., Zlotnik, S., Cas, R.A., 2011. Melt  
661 fracturing and healing: A mechanism for degassing and origin of silicic obsid-  
662 ian. Geology 39, 67–70. doi:10.1130/G31355.1.
- 663 Carey, S., Sigurdsson, H., 1985. The May 18, 1980 eruption of Mount St. Helens,  
664 2. Modeling of dynamics of the Plinian phase. J. Geophys. Res. 90, 2948–2958.  
665 doi:10.1029/JB090iB04p02948.

- 666 Carey, S., Sigurdsson, H., 1989. The intensity of plinian eruptions. *Bull. Vol-*  
667 *canol.* 51, 28–40. doi:10.1007/BF01086759.
- 668 Castro, J.M., Bindeman, I.N., Tuffen, H., Schipper, C.I., 2014. Explosive origin  
669 of silicic lava: Textural and  $\delta D-H_2O$  evidence for pyroclastic degassing during  
670 rhyolite effusion. *Earth. Planet. Sci. Lett.* 405, 52–61. doi:10.1016/j.epsl.  
671 2014.08.012.
- 672 Castro, J.M., Burgisser, A., Schipper, C.I., Mancini, S., 2012a. Mechanisms of  
673 bubble coalescence in silicic magmas. *Bull. Volcanol.* 74, 2339–2352. doi:10.  
674 1007/s00445-012-0666-1.
- 675 Castro, J.M., Cordonnier, B., Tuffen, H., Tobin, M.J., Parker, L., Martin, M.C.,  
676 Bechtel, H.A., 2012b. The role of melt-fracture degassing in defusing explosive  
677 rhyolite eruptions at volcan Chaiten. *Earth. Planet. Sci. Lett.* 333-334, 63–69.  
678 doi:10.1016/j.epsl.2012.04.024.
- 679 Castro, J.M., Manga, M., Martin, M.C., 2005. Vesiculation rates of obsidian  
680 domes inferred from  $H_2O$  concentration profiles. *Geophys. Res. Lett.* 32,  
681 L21307. doi:10.1029/2005GL024029.
- 682 Chiarabba, C., Amato, A., Evans, J.R., 1995. Variations on the NeHT high-  
683 resolution tomography method: a test of technique and results for Medicine  
684 Lake Volcano, northern California. *J. Geophys. Res.* 100, 4035–4052. doi:10.  
685 1029/94JB02771.
- 686 Clarke, A.B., Neri, A., Voight, B., Macedonio, G., Druitt, T.H., 2002. Compu-  
687 tational modelling of the transient dynamics of the August 1997 Vulcanian  
688 explosions at Soufrière Hills Volcano, Montserrat: Influence of initial con-  
689 duct conditions on near-vent pyroclastic dispersal. *Geol. Soc. Lond. Mem.* ,  
690 318–348doi:10.1144/GSL.MEM.2002.021.01.15.
- 691 Colucci, S., de' Michieli Vitturi, M., Neri, A., Palladino, D.M., 2014. An  
692 integrated model of magma chamber, conduit and column for the analy-

693 sis of sustained explosive eruptions. *Earth. Planet. Sci. Lett.* 404, 98–110.  
694 doi:10.1016/j.epsl.2014.07.034.

695 DeGroat-Nelson, P.J., Cameron, B.I., Fink, J.H., Holloway, J.R., 2001. Hydro-  
696 gen isotope analysis of rehydrated silicic lavas: implications for eruption mech-  
697 anisms. *Earth Planet. Sci. Lett.* 185, 331–341. doi:10.1016/S0012-821X(00)  
698 00379-4.

699 Degruyter, W., Bachmann, O., Burgisser, A., 2010. Controls on magma per-  
700 meability in the volcanic conduit during the climactic phase of the kos  
701 plateau tuff eruption (aegean arc). *Bulletin of Volcanology* 72, 63–74.  
702 doi:10.1007/s00445-009-0302-x.

703 Degruyter, W., Bachmann, O., Burgisser, A., Manga, M., 2012. The effects of  
704 outgassing on the transition between effusive and explosive silicic eruptions.  
705 *Earth Planet. Sci. Lett.* 349-350, 161–170. doi:10.1016/j.epsl.2012.06.  
706 056.

707 Dingwell, D.B., 1996. Volcanic Dilemma—Flow or Blow? *Science* 5278, 1054–  
708 1055. doi:10.1126/science.273.5278.1054.

709 Dobran, F., 1992. Nonequilibrium flow in volcanic conduits and applications to  
710 the eruptions of Mount St. Helens on May 18, 1980, and Vesuvius in A.D.  
711 79. *J. Volcanol. Geotherm. Res.* 49, 285–311. doi:10.1016/0377-0273(92)  
712 90019-A.

713 Donnelly-Nolan, J., Nathenson, M., Champion, D.E., Ramsey, D.W., Lowen-  
714 stern, J.B., Ewert, J.W., 2007. *Volcano Hazards Assessment for Medicine*  
715 *Lake Volcano, Northern California.* USGS-Scientific Investigation Report  
716 5174-A.

717 Donnelly-Nolan, J.M., Champion, D.E., Miller, C.D., Grove, T.L., Trimble,  
718 D.A., 1990. Post-11,000-Year Volcanism at Medicine Lake Volcano, Cascade  
719 Range, Northern California. *Journal of Geophysical Research* 95, 19,693–  
720 19,704. doi:10.1029/JB095iB12p19693.

- 721 Donnelly-Nolan, J.M., Grove, T.L., Lanphere, M.A., Champion, D.E., Ramsey,  
722 D.W., 2008. Eruptive history and tectonic setting of Medicine Lake Volcano,  
723 a large rear-arc volcano in the southern Cascades. *J. Volcanol. Geotherm.*  
724 *Res.* 177, 313–328. doi:10.1016/j.jvolgeores.2008.04.023.
- 725 Eichelberger, J., Westrich, H., 1981. Magmatic volatiles in explosive rhy-  
726 olitic eruptions. *Geophysical Research Letters* 8(7), 757–760. doi:10.1029/  
727 GL008i007p00757.
- 728 Eichelberger, J.C., Carrigan, C.R., Westrich, H.R., Price, R.H., 1986. Non-  
729 explosive silicic volcanism. *Nature* 323, 598–602. doi:10.1038/323598a0.
- 730 Epel’baum, M.B., Babashov, I.V., Salova, T.P., 1973. Surface tension of felsic  
731 magmatic melts at high temperatures and pressures. *Geochem. Int.* 10, 343–  
732 345.
- 733 Evans, J.R., Zucca, J.J., 1988. Active high-resolution seismic tomography of  
734 compressional wave velocity and attenuation structure at Medicine Lake Vol-  
735 cano, Northern California cascade range. *J. Geophys. Res.* 93, 15016–15036.  
736 doi:10.1029/JB093iB12p15016.
- 737 Feng, S., Halperin, B., Sen, P., 1987. Transport properties of continuum systems  
738 near the percolation threshold. *Physical Review B* 35, 197. doi:10.1103/  
739 PhysRevB.35.197.
- 740 Fowler, A.C., Scheu, B., Lee, W.T., McGuinness, J., 2010. A theoretical model  
741 of the explosive fragmentation of vesicular magma. *Proc. R. Soc. A* 466,  
742 731–752. doi:10.1098/rspa.2009.0382.
- 743 Gardner, J.E., Ketcham, R., 2011. Heterogeneous bubble nucleation on Fe-  
744 Ti oxide crystals in high-silica rhyolitic melts. *Contrib Mineral Petrol* 162,  
745 929–943. doi:10.1007/s00410-011-0632-5.
- 746 Gerlach, T.M., Westrich, H.R., Symonds, R.B., 1996. Pre-eruption vapor in  
747 magma of the climactic Mount Pinatubo eruption: source of the giant strato-  
748 spheric sulfur dioxide cloud, in: Newhall, C.G., Punongbayan, R. (Eds.), *Fire*

- 749 and Mud: Eruptions and Lahars of Mount Pinatubo, Philippines. University  
750 of Washington Press, Seattle, pp. 415–433.
- 751 Giachetti, T., Druitt, T., Burgisser, A., Arbaret, L., Galven, C., 2010. Bubble  
752 nucleation, growth and coalescence during the 1997 Vulcanian explosions of  
753 Soufriere Hills Volcano, Montserrat. *J. Volcanol. Geotherm. Res.* 193, 215–231.  
754 doi:10.1016/j.jvolgeores.2010.04.001.
- 755 Giachetti, T., Gonnermann, H.M., Gardner, J.E., Shea, T., Gouldstone, A.,  
756 2015. Discriminating secondary from magmatic water in rhyolitic matrix-  
757 glass of volcanic pyroclasts using thermogravimetric analysis. *Geochim. Cos-  
758 mochim. Acta* 148, 457–476. doi:10.1016/j.gca.2014.10.017.
- 759 Gonnermann, H.M., 2015. Magma fragmentation. *Annual Review of Earth and  
760 Planetary Sciences* 43. doi:10.1146/annurev-earth-060614-105206.
- 761 Gonnermann, H.M., Gardner, J.E., 2013. Homogeneous bubble nucleation in  
762 rhyolitic melt: Experiments and nonclassical theory. *Geochem. Geophys.  
763 Geosyst.* 14, 4758–4773. doi:10.1002/ggge.20281.
- 764 Gonnermann, H.M., Houghton, B.F., 2012. Magma degassing and fragmentation  
765 during the Plinian eruption of Novarupta, Alaska, 1912. *Geochem. Geophys.  
766 Geosyst.* 13(10), Q10009. doi:10.1029/2012GC004273.
- 767 Gonnermann, H.M., Manga, M., 2003. Explosive volcanism may not be  
768 an inevitable consequence of magma fragmentation. *Nature* 426, 432–435.  
769 doi:10.1038/nature02138.
- 770 Gonnermann, H.M., Manga, M., 2007. The fluid mechanics inside a vol-  
771 cano. *Annu. Rev. Fluid Mech.* 39, 321–356. doi:10.1146/annurev.fluid.  
772 39.050905.110207.
- 773 Grove, T.L., Donnelly-Nolan, J.M., 1986. The evolution of young silicic lavas  
774 at Medicine Lake Volcano, California: Implications for the origin of composi-  
775 tional gaps in calc-alkaline series lavas. *Contrib. Mineral. Petrol.* 92, 281–302.  
776 doi:10.1007/BF00572157.

- 777 Grove, T.L., Donnelly-Nolan, J.M., Housh, T., 1997. Magmatic processes that  
778 generated the rhyolite of Glass Mountain, Medicine Lake volcano, N. Califor-  
779 nia. *Contrib. Mineral. Petrol.* 127, 205–223. doi:10.1007/s004100050276.
- 780 Haar, L., Gallagher, J.S., Kell, G.S., 1984. Nbs/nrc steam tables: Thermody-  
781 namic and transport properties and computer programs for vapor and liquid  
782 states of water in si units, 320 p. Hemisphere, Washington, DC .
- 783 Hamada, M., Laporte, D., Cluzel, N., Koga, K.T., Kawamoto, T., 2010. Sim-  
784 ulating bubble number density of rhyolitic pumices from plinian eruptions:  
785 constraints from fast decompression experiments. *Bulletin of Volcanology* 72,  
786 735–746. doi:10.1007/s00445-010-0353-z.
- 787 Heiken, G., 1978. Plinian-type eruptions in the Medicine Lake Highland, Cali-  
788 fornia, and the nature of the underlying magma. *J. Volcanol. Geotherm. Res.*  
789 4, 375–402. doi:10.1016/0377-0273(78)90023-9.
- 790 Hildreth, W., Fierstein, J., 2012. The Novarupta-Katmai eruption of 1912?  
791 Largest eruption of the twentieth century. Centennial perspectives: U.S.  
792 Geological Survey Professional Paper 1791, 278 pp.
- 793 Hui, H., Zhang, Y., 2007. Toward a general viscosity equation for natural  
794 anhydrous and hydrous silicate melts. *Geochim. Cosmochim. Acta* 71, 403–  
795 416. doi:10.1016/j.gca.2006.09.003.
- 796 Hurwitz, S., Navon, O., 1994. Bubble nucleation in rhyolitic melts: Experiments  
797 at high-pressure, temperature, and water-content. *Earth. Planet. Sci. Lett.*  
798 122, 267–280. doi:10.1016/0012-821X(94)90001-9.
- 799 Ichihara, M., Rittel, D., Sturtevant, B., 2002. Fragmentation of a porous vis-  
800 coelastic material: implications to magma fragmentation. *Journal of Geo-*  
801 *physical Research: Solid Earth* (1978–2012) 107, ECV–8. doi:10.1029/  
802 2001JB000591.

- 803 Jaupart, C., 1998. Gas loss from magmas through a conduit walls during erup-  
804 tion. *Geol. Soc. Lond. Spec. Pub.* 145, 73–90. doi:10.1144/GSL.SP.1996.  
805 145.01.05.
- 806 Jaupart, C., Allègre, C.J., 1991. Gas content, eruption rate and instabilities of  
807 eruption regime in silicic volcanoes. *Earth Planet. Sci. Lett.* 102, 413–429.  
808 doi:10.1016/0012-821X(91)90032-D.
- 809 Kerrick, D.M., Jacobs, G.K., 1981. A modified Redlich-Kwong equation for  
810 H<sub>2</sub>O, CO<sub>2</sub> and H<sub>2</sub>O-CO<sub>2</sub> mixtures at elevated pressures and temperatures.  
811 *Am. J. Sci.* 281, 735–767.
- 812 Klug, C., Cashman, K.V., 1994. Vesiculation of May 18, 1980 Mount St. Helens  
813 magma. *Geology* 22, 468–472. doi:10.1130/0091-7613.
- 814 Klug, C., Cashman, K.V., 1996. Permeability development in vesiculat-  
815 ing magmas: implications for fragmentation. *Bull. Volcanol.* 58, 87–100.  
816 doi:10.1007/s004450050128.
- 817 Klug, C., Cashman, K.V., Bacon, C.R., 2002. Structure and physical char-  
818 acteristics of pumice from climatic eruption of Mt. Mazama (Crater Lake),  
819 Oregon. *Bull. Volcanol.* 64, 486 – 501. doi:10.1007/s00445-002-0230-5.
- 820 Koyaguchi, T., 2005. An analytical study for 1-dimensional steady flow in vol-  
821 canic conduits. *J. Volcanol. Geotherm. Res.* 143, 29–52. doi:10.1016/j.  
822 jvolgeores.2004.09.009.
- 823 Lensky, N., Navon, O., Lyakhovsky, V., 2004. Bubble growth during de-  
824 compression of magma: experimental and theoretical investigation. *Journal of Volcanology and Geothermal Research* 129, 7–22. doi:doi:10.1016/  
825 S0377-0273(03)00229-4.  
826 S0377-0273(03)00229-4.
- 827 Lensky, N.G., Lyakhovsky, V., Navon, O., 2001. Radial variations of melt vis-  
828 cosity around growing bubbles and gas overpressure in vesiculating magmas.  
829 *Earth. Planet. Sci. Lett.* 186, 1–6. doi:10.1016/S0012-821X(01)00227-8.

- 830 Liu, Y., Zhang, Y., Behrens, H., 2005. Solubility of H<sub>2</sub>O in rhyolitic melts at  
831 low pressures and a new empirical model for mixed H<sub>2</sub>O-CO<sub>2</sub> solubility in  
832 rhyolitic melts. *J. Volcanol. Geotherm. Res.* 143, 219–235. doi:10.1016/j.  
833 *jvolgeores*.2004.09.019.
- 834 Lyakhovskiy, V., Hurwitz, S., Navon, O., 1996. Bubble growth in rhyolitic melts:  
835 Experimental and numerical investigation. *Bull. Volcanol.* 58, 19–32. doi:10.  
836 1007/s004450050122.
- 837 Macedonio, G., Neri, A., Marti, J., Folch, A., 2005. Temporal evolution of flow  
838 conditions in sustained magmatic explosive eruptions. *J. Volcanol. Geotherm.*  
839 *Res.* 143, 153–172. doi:10.1016/j.*jvolgeores*.2004.09.015.
- 840 Mader, H., Llewellyn, E., Mueller, S., 2013. The rheology of two-phase magmas:  
841 A review and analysis. *Journal of Volcanology and Geothermal Research* 257,  
842 135–158. doi:10.1016/j.*jvolgeores*.2013.02.014.
- 843 de Maisonrouve, C.B., Bachmann, O., Burgisser, A., 2009. Characterization of  
844 juvenile pyroclasts from the Kos Plateau Tuff (Aegean Arc): insights into the  
845 eruptive dynamics of a large rhyolitic eruption. *Bull. Volcanol.* 71, 643–658.  
846 doi:10.1007/s00445-008-0250-x.
- 847 Mangan, M., Sisson, T., 2000. Delayed, disequilibrium degassing in rhyolite  
848 magma: Decompression experiments and implications for explosive volcan-  
849 ism. *Earth. Planet. Sci. Lett.* 183, 441–455. doi:10.1016/S0012-821X(00)  
850 00299-5.
- 851 Mastin, L., Guffanti, M., Servranckx, R., Webley, P., Barsotti, S., Dean, K., Du-  
852 rant, A., Ewert, J., Neri, A., Rose, W., et al., 2009. A multidisciplinary effort  
853 to assign realistic source parameters to models of volcanic ash-cloud trans-  
854 port and dispersion during eruptions. *Journal of Volcanology and Geothermal*  
855 *Research* 186, 10–21. doi:10.1016/j.*jvolgeores*.2009.01.008.
- 856 Mastin, L.G., 2002. Insights into volcanic conduit flow from an open-source

- 857 numerical model. *Geochem. Geophys. Geosyst.* 3, 1037. doi:10.1029/  
858 2001GC000192.
- 859 Mastin, L.G., Ghiorso, M.S., 2000. A Numerical Program for Steady-State Flow  
860 of Magma-Gas Mixtures through Vertical Eruptive Conduits. U.S. Geol. Surv.  
861 Open File Rep. 00-209, 53.
- 862 McBirney, A.R., Murase, T., 1970. Factors governing the formation of pyroclas-  
863 tic rocks. *Bull. Volcanol.* 34, 372–384. doi:10.1007/BF02596762.
- 864 McGuinness, M., Scheu, B., Fowler, A., 2012. Explosive fragmentation criteria  
865 and velocities for vesicular magma. *Journal of Volcanology and Geothermal*  
866 *Research* 237, 81–96. doi:10.1016/j.jvolgeores.2012.05.019.
- 867 Melnik, O., 2000. Dynamics of two-phase conduit flow of high-viscosity gas-  
868 saturated magma: large variations of sustained explosive eruption intensity.  
869 *Bull. Volcanol.* 62, 153–170. doi:10.1007/s004450000072.
- 870 Melnik, O., Barmin, A.A., Sparks, R.S.J., 2005. Dynamics of magma flow in-  
871 side volcanic conduits with bubble overpressure buildup and gas loss through  
872 permeable magma. *J. Volcanol. Geotherm. Res.* 143, 53–68. doi:10.1029/  
873 2004JB003183.
- 874 Mitchell, K.L., 2005. Coupled conduit flow and shape in explosive volcanic  
875 eruptions. *Journal of volcanology and geothermal research* 143, 187–203.  
876 doi:10.1016/j.jvolgeores.2004.09.017.
- 877 Moitra, P., Gonnermann, H.M., Houghton, B.F., T., G., 2013. Relating vesicle  
878 shapes in pyroclasts to eruption styles. *Bull. Volcanol.* 75, 691. doi:10.1007/  
879 s00445-013-0691-8.
- 880 Mourtada-Bonnefoi, C.C., Laporte, D., 2004. Kinetics of bubble nucleation in  
881 a rhyolitic melt: An experimental study of the effect of ascent rate. *Earth.*  
882 *Planet. Sci. Lett.* 218, 521–537. doi:10.1016/S0012-821X(03)00684-8.

- 883 Mueller, S., Melnik, O., Spieler, O., Scheu, B., Dingwell, D.B., 2005. Perme-  
884 ability and degassing of dome lavas undergoing rapid decompression: An  
885 experimental determination. *Bull. Volcanol.* 67, 526–538. doi:10.1007/  
886 s00445-004-0392-4.
- 887 Mueller, S., Scheu, B., Spieler, O., Dingwell, D.B., 2008. Permeability control  
888 on magma fragmentation. *Geology* 36, 399–402. doi:10.1130/G24605A.1.
- 889 Namiki, A., Manga, M., 2005. Response of a bubble bearing viscoelastic fluid to  
890 rapid decompression: implications for explosive volcanic eruptions. *Earth and*  
891 *Planetary Science Letters* 236, 269–284. doi:10.1016/j.epsl.2005.02.045.
- 892 Nguyen, C.T., Gonnermann, H.M., Chen, Y., Huber, C., Maiorano, A.A.,  
893 Gouldstone, A., Dufek, J., 2013. Film drainage and the lifetime of bubbles.  
894 *Geochem. Geophys. Geosyst.* 14, 3616–3631. doi:10.1002/ggge.20198.
- 895 Nguyen, C.T., Gonnermann, H.M., Houghton, B.F., 2014. Explosive to effusive  
896 transition during the largest volcanic eruption of the 20th century (Novarupta  
897 1912, Alaska). *Geology* doi:10.1130/G35593.1.
- 898 Ni, H., Zhang, Y., 2008. H<sub>2</sub>O diffusion models in rhyolitic melt with new high  
899 pressure data. *Chem Geol.* 250, 68–78. doi:10.1016/j.chemgeo.2008.02.  
900 011.
- 901 Okumura, S., Nakamura, M., Takeuchi, S., Tsuchiyama, A., Nakano, T., Ue-  
902 sugi, K., 2009. Magma deformation may induce non-explosive volcanism via  
903 degassing through bubble networks. *Earth Planet. Sci. Lett.* 281, 267–274.  
904 doi:10.1016/j.epsl.2009.02.036.
- 905 Okumura, S., Nakamura, M., Tsuchiyama, A., 2006. Shear-induced bubble coa-  
906 lesence in rhyolitic melts with low vesicularity. *Geophysical research letters*  
907 33. doi:10.1029/2006GL027347.
- 908 Pal, R., 2003. Rheological behavior of bubble-bearing magmas. *Earth. Planet.*  
909 *Sci. Lett.* 207, 165–179. doi:10.1016/S0012-821X(02)01104-4.

- 910 Papale, P., 1999. Modeling of the solubility of a two-component H<sub>2</sub>O + CO<sub>2</sub> fluid  
911 in silicate liquids. *Am. Mineral.* 84, 477–492. doi:10.1007/s004100050247.
- 912 Papale, P., 2001. Dynamics of magma flow in volcanic conduits with variable  
913 fragmentation efficiency and nonequilibrium pumice degassing. *Journal of*  
914 *Geophysical Research: Solid Earth (1978–2012)* 106, 11043–11065. doi:10.  
915 1029/2000JB900428.
- 916 Papale, P., 2005. Determination of total h<sub>2</sub>o and co<sub>2</sub> budgets in evolving mag-  
917 mas from melt inclusion data. *Journal of Geophysical Research: Solid Earth*  
918 (1978–2012) 110. doi:10.1029/2004JB003033.
- 919 Polacci, M., de Maisonneuve, C.B., Giordano, D., Piochi, M., Manicini, L.,  
920 Degruyter, W., Bachmann, O., 2014. Permeability measurements of Campi  
921 Flegrei pyroclastic products: An example from the Campanian Ignimbrite  
922 and Monte Nuovo eruptions. *J. Volcanol. Geotherm. Res.* 272, 16–22. doi:10.  
923 1016/j.jvolgeores.2013.12.002.
- 924 Proussevitch, A.A., Sahagian, D.L., Anderson, A.T., 1993a. Dynamics of diffu-  
925 sive bubble growth in magmas: Isothermal case. *J. Geophys. Res.* 98, 22,283–  
926 22,307. doi:10.1029/93JB02027.
- 927 Proussevitch, A.A., Sahagian, D.L., Kutolin, V.A., 1993b. Stability of foams  
928 in silicate melts. *J. Volcanol. Geotherm. Res.* 59, 161–178. doi:10.1016/  
929 0377-0273(93)90084-5.
- 930 Rallison, J., 1984. The deformation of small viscous drops and bubbles in shear  
931 flows. *Annual Review of Fluid Mechanics* 16, 45–66. doi:10.1146/annurev.  
932 fl.16.010184.000401.
- 933 Rust, A., Manga, M., 2002. Effects of bubble deformation on the viscosity of  
934 dilute suspensions. *Journal of Non-Newtonian Fluid Mechanics* 104, 53–63.  
935 doi:10.1016/S0377-0257(02)00013-7.

- 936 Rust, A.C., Cashman, K.V., 2004. Permeability of vesicular silicic magma:  
937 inertial and hysteresis effects. *Earth Planet. Sci. Lett.* 228, 93–107. doi:10.  
938 1016/j.epsl.2004.09.025.
- 939 Rust, A.C., Cashman, K.V., 2011. Permeability controls on expansion and  
940 size distributions of pyroclasts. *J. Geophys. Res.* 116, B11202. doi:10.1029/  
941 2011JB008494.
- 942 Saar, M., Manga, M., 1999. Permeability - porosity relationship in vesicular  
943 basalts. *Geophys. Res. Lett.* 26, 111–114. doi:10.1029/1998GL900256.
- 944 Sahimi, M., 1994. *Applications of Percolation Theory*. Taylor and Francis,  
945 London. doi:10.1002/nadc.19940421121.
- 946 Shea, T., Gurioli, L., Houghton, B.F., 2012. Transitions between fall phases and  
947 pyroclastic density currents during the AD 79 eruption at Vesuvius: building a  
948 transient conduit model from the textural and volatile record. *Bull. Volcanol.*  
949 74, 2363–2381. doi:10.1007/s00445-012-0668-z.
- 950 Shea, T., Hellebrand, E., Gurioli, L., Tuffen, H., 2014. Conduit- to Localized-  
951 scale Degassing during Plinian Eruptions: Insights from Major Element and  
952 Volatile (Cl and H<sub>2</sub>O) Analyses within Vesuvius AD 79 Pumice. *J. Pet.* 0(0),  
953 1–30. doi:10.1093/petrology/egt069.
- 954 Shea, T., Houghton, B.F., Gurioli, L., Cashman, K.V., Hammer, J.E., Hob-  
955 den, B.J., 2010. Textural studies of vesicles in volcanic rocks: An integrated  
956 methodology. *J. Volcanol. Geotherm. Res.* 190, 270–289. doi:10.1016/j.  
957 jvolgeores.2010.02.013.
- 958 Slezin, Y.B., 2003. The mechanism of volcanic eruptions (a steady state  
959 approach). *Journal of Volcanology and Geothermal Research* 122, 7–50.  
960 doi:10.1016/S0377-0273(02)00464-X.
- 961 Sparks, R.S.J., 1978. The dynamics of bubble formation and growth in magmas.  
962 *J. Volcanol. Geotherm. Res.* 3, 1–37. doi:10.1016/0377-0273(78)90002-1.

- 963 Sparks, R.S.J., 2003. Dynamics of magma degassing. *Geol. Soc. Lond. Spec.*  
964 *Pub.* 213, 5–22. doi:10.1144/GSL.SP.2003.213.01.02.
- 965 Spieler, O., Kennedy, B., Kueppers, U., Dingwell, D.B., Scheu, B., Taddeucci,  
966 J., 2004. The fragmentation threshold of pyroclastic rocks. *Earth Planet. Sci.*  
967 *Lett.* 226, 139–148. doi:10.1016/j.epsl.2004.07.016.
- 968 Stasiuk, M.V., Barclay, J., Carroll, M.R., Jaupart, C., Ratté, J.C., Sparks,  
969 R.S.J., Tait, S.R., 1996. Degassing during magma ascent in the mule  
970 creek vent (usa). *Bulletin of Volcanology* 58, 117–130. doi:10.1007/  
971 s004450050130.
- 972 Stevenson, R.J., Dingwell, D.B., Webb, S.L., Sharp, T.G., 1996. Viscosity of  
973 microlite-bearing rhyolitic obsidians: an experimental study. *Bull. Volcanol.*  
974 58, 298–309. doi:10.1007/s004450050141.
- 975 Stone, H., 1994. Dynamics of drop deformation and breakup in viscous fluids.  
976 *Annual Review of Fluid Mechanics* 26, 65–102. doi:10.1146/annurev.fl.  
977 26.010194.000433.
- 978 Takeuchi, S., Nakashima, S., Tomiya, A., 2008. Permeability measurements  
979 of natural and experimental volcanic materials with a simple permeame-  
980 ter: toward an understanding of magmatic degassing processes. *J. Volcanol.*  
981 *Geotherm. Res.* 177, 329–339. doi:10.1016/j.jvolgeores.2008.05.010.
- 982 Tatlock, D., Flanagan, F., Bastron, H., Berman, S., Sutton Jr, A., 1976. Rhy-  
983 olite, rgm-1, from glass mountain, california. *Descriptions and Analyses of*  
984 *Eight New USGS Rock Standards*, 11–14.
- 985 Taylor, B.E., Eichelberger, J., Westrich, H., 1983. Hydrogen isotopic evidence  
986 of rhyolitic magma degassing during shallow intrusion and eruption. *Nature*  
987 306, 541–545. doi:10.1038/306541a0.
- 988 Toramaru, A., 1988. Formation of propagation pattern in two-phase flow  
989 systems with applications to volcanic eruptions. *Geophys. J.* 95, 613–623.  
990 doi:10.1111/j.1365-246X.1988.tb06707.

- 991 Toramaru, A., 1990. Measurement of bubble size distribution in vesiculated  
992 rocks with implications for quantitative estimation of eruption processes. *J.*  
993 *Volcanol. Geotherm. Res.* 43, 71–90. doi:10.1016/0377-0273(90)90045-H.
- 994 Tuffen, H., Dingwell, D., 2005. Fault textures in volcanic conduits: evidence for  
995 seismic trigger mechanisms during silicic eruptions. *Bulletin of Volcanology*  
996 67, 370–387. doi:10.1007/s00445-004-0383-5.
- 997 Tuffen, H., Dingwell, D.B., Pinkerton, H., 2003. Repeated fracture and healing  
998 of silicic magma generate flow banding and earthquakes? *Geology* 31, 1089–  
999 1092. doi:10.1130/G19777.1.
- 1000 Wallace, P., 2005. Volatiles in subduction zone magmas: concentrations and  
1001 fluxes based on melt inclusion and volcanic gas data. *J. Volcanol. Geotherm.*  
1002 *Res.* 140, 217–240. doi:10.1016/j.jvolgeores.2004.07.023.
- 1003 Westrich, H.R., Eichelberger, J.C., 1994. Gas transport and bubble collapse  
1004 in rhyolitic magma: an experimental approach. *Bull. Volcanol.* 56, 447–458.  
1005 doi:10.1007/BF00302826.
- 1006 Wilson, L., Sparks, R.S.J., Walker, G.P.L., 1980. Explosive volcanic eruptions  
1007 - IV. The control of magma properties and conduit geometry on eruption  
1008 column behaviour. *Geophys. J. R. astr. Soc.* 63, 117–148. doi:10.1111/  
1009 j.1365-246X.1980.tb02613.x.
- 1010 Woods, A., Koyaguchi, T., 1994. Transitions between explosive and effusive  
1011 eruptions of silicic magmas. *Nature* 370, 641–644. doi:10.1038/370641a0.
- 1012 Woods, A.W., 1995. The dynamics of explosive volcanic eruptions. *Rev. Geo-*  
1013 *phys.* 33, 495–530. doi:10.1029/95RG02096.
- 1014 Wright, H., Cashman, K., Gottesfeld, E., Roberts, J., 2009. Pore structure  
1015 of volcanic clasts: Measurements of permeability and electrical conductivity.  
1016 *Earth Planet. Sci. Lett.* 280, 93–104. doi:10.1016/j.epsl.2009.01.023.

- 1017 Zhang, Y., 1999. A criterion for the fragmentation of bubbly magma based on  
1018 brittle failure theory. *Nature* 402, 648–650. doi:10.1038/45210.
- 1019 Zhang, Y., Xu, Z., Zhu, M., Wang, H., 2007. Silicate melt properties and  
1020 volcanic eruptions. *Rev. Geophys.* 45, RG4004. doi:10.1029/2006RG000216.

Table 1: Units, description, and eventual value and origin of the symbols used in this study.

Symbol	Unit	Value	Description	Source/Equation
$a$	m		Conduit radius	
$b$			Empirical pre-exponential term of $k - \phi_t$ power-law relationship	Equation (2)
$c$			Empirical exponent of $k - \phi_t$ power-law relationship	Equation (2)
$C$	wt%		Concentration of water in the melt	
$C_{F_g}$	wt%		Solubility of water	Liu et al. (2005)
$D$	$\text{m}^2\text{s}^{-1}$		Water diffusivity	Ni and Zhang (2008)
$f$			Friction factor	Equation (6)
$f_0$		0.02	Friction factor for turbulent-flow conditions	Wilson et al. (e.g., 1980)
$g$	$\text{m}\cdot\text{s}^{-2}$	9.81	Acceleration due to gravity	
$k$	$\text{m}^2$		Viscous (Darcian) permeability	
$k_2$	m		Inertial (non-Darcian) permeability	
$L$	m		Length over which permeable outgassing occurs	
$M$			Mach number	
$N$	$\text{m}^{-3}$	$4 \times 10^{14}$	Bubble number density in the melt	This study
$\dot{P}_m$	$\text{Pa}\cdot\text{s}^{-1}$		Decompression rate	
$P_m$	Pa		Confining (ambient, melt) pressure	
$P_g$	Pa		Gas pressure inside bubble	
$\text{Pe}_k$			Péclet number for permeable outgassing	
$\text{Pe}_\eta$			Péclet number for viscosity	
$q_k$	$\text{m}\cdot\text{s}^{-1}$		Volumetric flux of gas due to o.s.d (per unit volume of magma)	
$Q$	$\text{kg}\cdot\text{s}^{-1}$		Mass discharge rate of magma during the eruption	
$r$	m		Radial coordinate for bubble growth modeling	
$R$	m		Average radius of the bubble	
$\text{Re}$			Reynolds number	
$S$	m		Outer radius of the shell of melt surrounding each bubble	
$t$	s		Time	
$u$	$\text{m}\cdot\text{s}^{-1}$		Magma ascent velocity	
$z$	m		Vertical coordinate (depth)	
$\alpha$		0.9	Empirical constant used to iteratively include open-system degassing	Equation (14)
$\Delta P$	Pa	$P_g - P_m$	Gas overpressure in bubble	
$\Delta P_f$	Pa		Fragmentation criterion	Mueller et al. (2008)
$\gamma$	$\text{N}\cdot\text{m}^{-1}$	0.06	Surface tension	Epel'baum et al. (1973)
$\eta$	$\text{Pa}\cdot\text{s}$		Magma viscosity	Pal (2003)
$\eta_e$	$\text{Pa}\cdot\text{s}$		Effective viscosity of the melt	Lensky et al. (2001)
$\eta_g$	$\text{Pa}\cdot\text{s}$		Viscosity of the water vapor	Haar et al. (1984)
$\eta_m$	$\text{Pa}\cdot\text{s}$		Viscosity of the melt	Hui and Zhang (2007)
$\phi_c$			Volume fraction of interconnected gas bubbles in magma	
$\phi_{cr}$			Percolation threshold	
$\phi_t$			Total volume fraction of gas in magma (total porosity)	
$\rho$	$\text{kg}\cdot\text{m}^{-3}$		Density of the magma	
$\rho_g$	$\text{kg}\cdot\text{m}^{-3}$		Density of the supercritical water	Kerrick and Jacobs (1981)
$\rho_m$	$\text{kg}\cdot\text{m}^{-3}$	2,430	Density of GM rhyolitic melt	Giachetti et al. (2015)
$\sigma_m$	$\text{Pa}^{-1}$	$1.54 \times 10^6$	Effective tensile strength of the matrix skeleton	Mueller et al. (2008)
$\tau_{dec}$	s		Decompression Time-scale	
$\tau_{dif}$	s		Time-scale for water diffusion in melt	
$\tau_{exp}$	s		Time-scale for pyroclast expansion	
$\tau_k$	s		Time-scale for permeable outgassing	
$\tau_\eta$	s		Viscous time-scale	

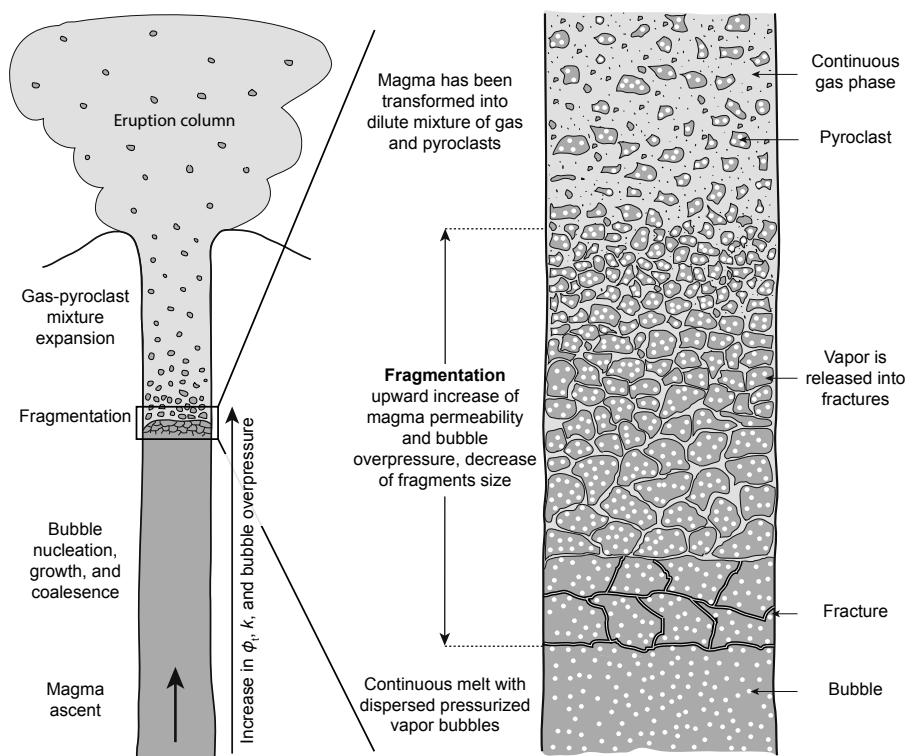


Figure 1: Schematic conceptual model of brittle magma fragmentation during a Plinian eruption. Decompression of magma during ascent and pressure-dependent solubility lead to the nucleation and growth of vapor bubbles of magmatic volatiles. The vapor inside the bubbles decompresses at a slower rate than the ambient pressure decreases, because the relatively high viscosity of the melt resists bubble growth. Bubbles thus become over-pressurized. When this overpressure exceeds a threshold, the bubbly magma fragments into pyroclasts. During this process the fractured magma becomes fluidized by expansion and release of the pressurized vapor from within the bubbles into a gas-pyroclast mixture, which jets into the Earth's atmosphere.

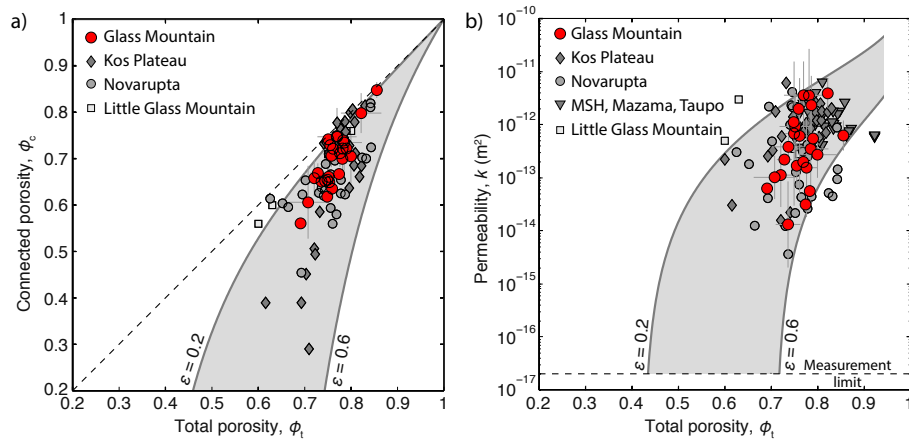


Figure 2: **(a)** Connected porosity,  $\phi_c$ , vs. total porosity,  $\phi_t$ , for Plinian pumices. Error bar for Glass Mountain pumices is one standard deviation of the measurements made on each sample (Section 3). **(b)** Darcian permeability,  $k$ , as a function of total porosity. Measurement limit is  $\sim 10^{-17} \text{ m}^2$ . Shaded gray area is predicted permeabilities based on percolation modeling of  $\phi_c$  and  $\phi_t$  (Appendix C) for values of  $\epsilon = 0.2 - 0.6$  (shaded gray area). Red symbols represent samples analyzed in this study and gray symbols are data from other Plinian eruptions: Kos Plateau (de Maisonneuve et al., 2009), Novarupta (Nguyen et al., 2014), Mount Saint Helens (MSH), Mount Mazama, Taupo (Klug and Cashman, 1996), Plinian phase preceding Little Glass Mountain rhyolitic flow (Rust and Cashman, 2004).

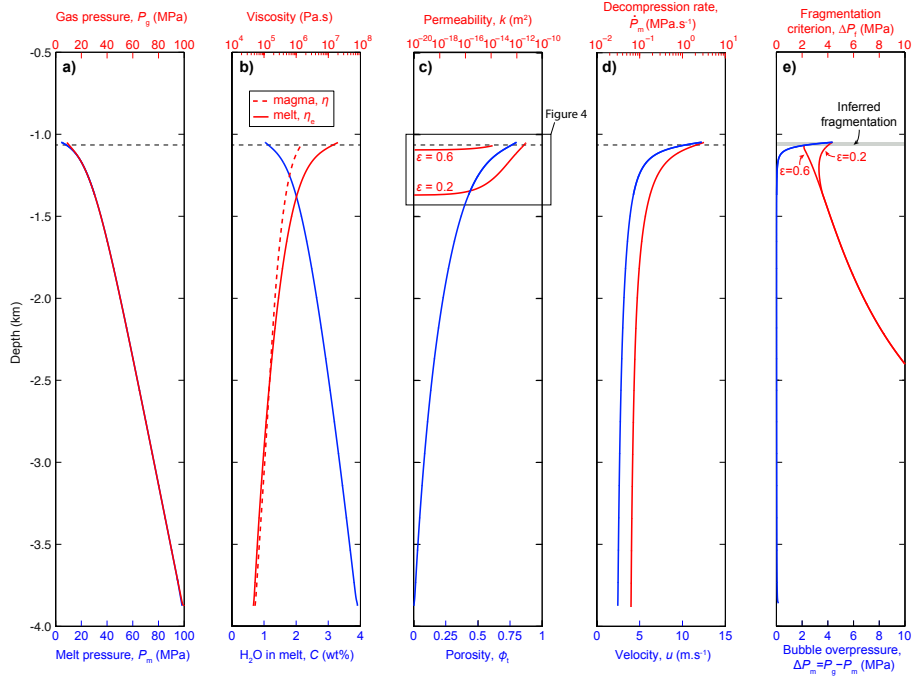


Figure 3: Illustrative typical open-system degassing model results for a mass discharge rate of  $1.1 \times 10^7 \text{ kg.s}^{-1}$  and a conduit radius of 24 m. Here, a value of  $\epsilon = 0.2$  is used to calculate  $k$  from  $\phi_t$ . **(a)** As magma rises in the conduit, the pressure of the melt,  $P_m$ , decreases from 100 MPa to approximately 9 MPa at fragmentation. **(b)** Water diffuses from the melt into the bubbles because of pressure-dependent solubility. As a consequence effective melt viscosity,  $\eta_e$ , and magma viscosity,  $\eta$ , increase. Because of increasing capillary number and magma porosity,  $\eta$  is somewhat smaller than  $\eta_e$  above approximately -2.5 km (cf., Pal, 2003). **(c)** Decreasing pressure and exsolution of  $\text{H}_2\text{O}$  result in an increase in the volume fraction of bubbles,  $\phi_t$ , and in permeability,  $k$ . **(d)** The ensuing decrease in magma density requires magma velocity,  $u$ , to increase. In combination with increasing  $\eta$ , this results in an increase in the absolute value of decompression rate,  $\dot{P}_m$ . **(e)** The increase in melt viscosity also affects bubble growth, consequently  $P_m$  decreases faster than  $P_g$ , until the overpressure in the bubble,  $\Delta P$ , reaches the fragmentation criterion,  $\Delta P_f$ . Plotted  $\Delta P_f$  are calculated using Equation (2) and either  $\epsilon = 0.2$  or  $\epsilon = 0.6$ .

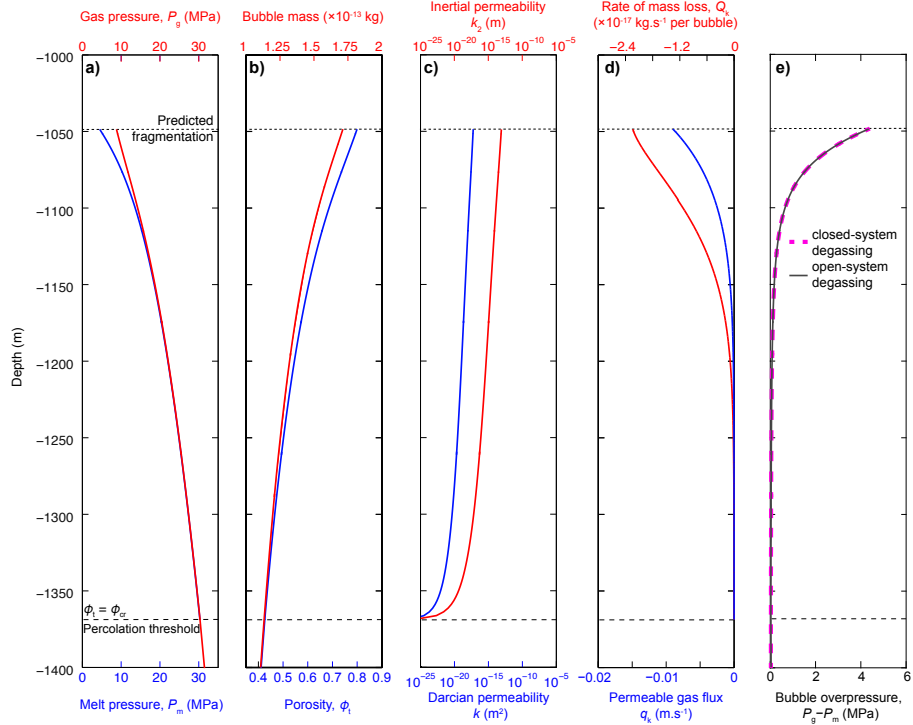


Figure 4: Results of the o.s.d numerical modeling obtained for a mass discharge rate of  $1.1 \times 10^7 \text{ kg.s}^{-1}$  and a conduit radius of 24 m (a-d) and comparison with the results of a c.s.d model obtained using the same initial parameters (e). Calculations were made using  $\epsilon = 0.2$  to calculate  $k$  from  $\phi_t$ . The dashed line at the bottom of each graph symbolizes the percolation threshold. The dashed line at the top of each graph represents the expected depth of fragmentation. (a) Melt and gas pressure. (b) Porosity and mass of gas in the bubble. (c) Darcian and inertial permeabilities. (d) Permeable gas flux per unit volume of magma and rate of mass loss due to o.s.d per unit volume of bubble. (e) Bubble overpressure for closed-system degassing case (dashed magenta) and open-system degassing case (solid dark gray), showing that upward open system degassing through the network of interconnected bubbles has a negligible effect on bubble overpressure.

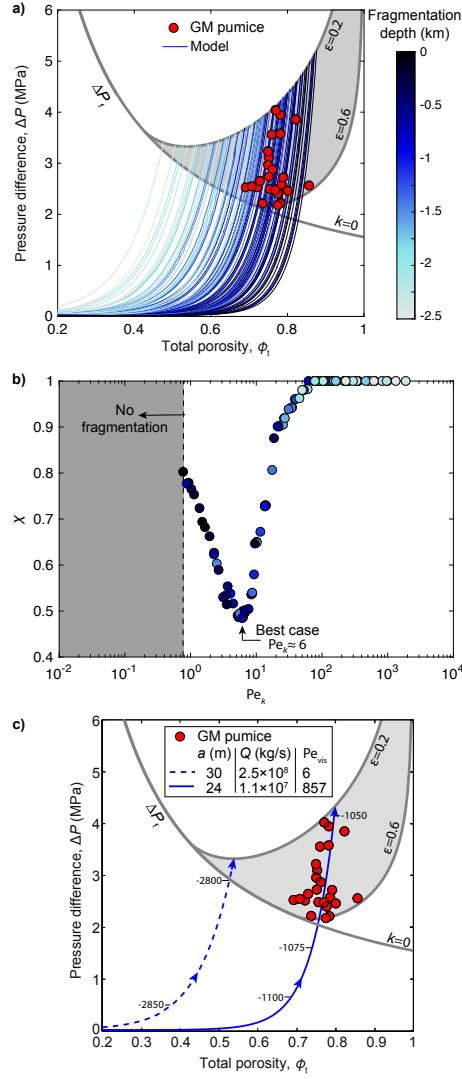


Figure 5: Results of the numerical modeling. **(a)** Estimated gas overpressure at fragmentation (red filled circles) using measured sample porosity and permeability in Equation (15). The gray shaded area indicates the range of  $\Delta P_f$  based on percolation modeling with  $0.2 \leq \epsilon \leq 0.6$ . Predicted eruption trajectories from the numerical model (curves) for different combinations of  $Q$  and  $a$ , using fragmentation depth obtained for  $\epsilon = 0.2$  as color code. Cases for which magma reaches the surface before magma fragmentation, or those for which predicted fragmentation occurs below a depth of -2.5 km, are not shown. **(b)** Root-mean-square error,  $\chi$  (Equation (26)) as a function of  $Pe_\eta$  (Equation (20)). The minimum  $\chi$  is obtained for  $Pe_\eta \approx 6$ . For  $Pe_\eta \lesssim 0.8$  magma reaches the surface before it fragments. The model predicts an overall decrease of the fragmentation depth with increasing  $Pe_\eta$ . **(c)** Example of *best case* scenario (solid blue curve) and case for which fragmentation would occur at a depth of about -2.8 km and a porosity of about 0.55 (dashed line). The black ticks along the curves mark depth in meters.

1021 **Appendix A. Viscous and inertial permeabilities**

Permeability data were acquired using two flow meters (Figure A.1a-b). The viscous and inertial permeabilities of the sub-samples were obtained by finding the  $k$  and  $k_2$  in Equation (1) that allow for the best fit to the measured flows (Figure A.1a-b), in a least squares sense. In Equation (1),  $P_0$  and  $P_1$  are equal to 101,325 Pa,  $\eta_g$  is  $1.86 \times 10^{-5}$  Pa.s and  $\rho_g$  equals  $1.18 \text{ kg.m}^{-3}$ . Figure A.1c shows the value of the misfit, defined as

$$\sqrt{\sum_{i=1}^n \left( \frac{q_{\text{mes}} - q_{\text{pred}}}{q_{\text{mes}}} \right)^2}, \quad (\text{A.1})$$

1022 where  $q_{\text{mes}}$  and  $q_{\text{pred}}$  are the measured and predicted volume fluxes respectively  
 1023 and  $n$  is the number of data acquired, as a function of the values of  $k$  and  $k_2$  for  
 1024 one sample. The best values of  $k$  and  $k_2$  are those for which the value of misfit  
 is minimum (Figure A.1c).

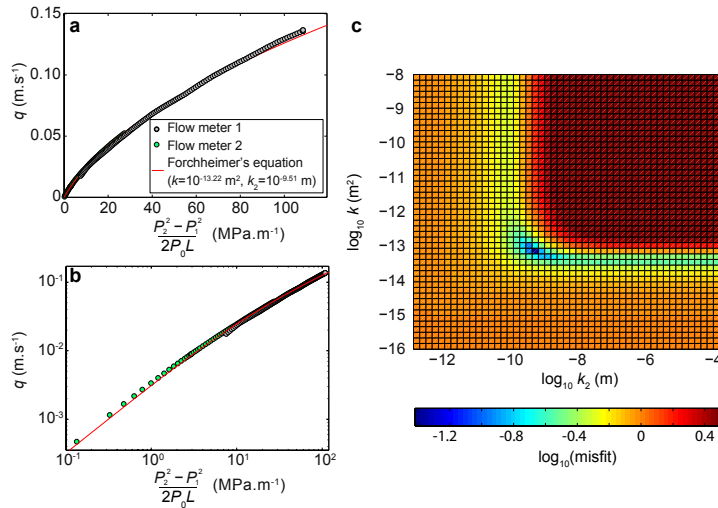


Figure A.1: Example of fitting flow data to estimate pyroclast permeability. (a – b) Measured data and best fit obtained shown as the flux as a function of the modified pressure gradient, in linear (a) and log-log (b) scales. (c) Misfit as a function of the  $k$  and  $k_2$  used to calculate the flux as a function of the pressure gradient.

1025

## 1026 **Appendix B. Bubble Size Distribution**

1027 The BSD of one typical GM pumice was measured by image analysis. A  
1028 representative sample ( $\phi_t = 0.75$ ,  $\phi_c = 0.66$ ) was thin-sectioned and Scanning  
1029 Electron Microscope (SEM) images of this section were taken at magnifications  
1030 of  $\times 80$  (1 image) and  $\times 300$  (3 images). Grayscale images (Figure B.1a) were  
1031 manually transformed into binary images and the bubble walls separating re-  
1032 cently coalesced vesicles were reconstructed (e.g., Toramaru, 1990; Giachetti  
1033 et al., 2010). The images were analyzed with the program FOAMS developed  
1034 by Shea et al. (2010). We used a minimum resolvable diameter of 5 pixels,  
1035 which corresponds to a vesicle of approximately  $2.4 \mu\text{m}$  on the  $\times 300$  images. A  
1036 minimum resolvable diameter of 5 pixels for this type of highly porous pyroclast  
1037 allows to discard noise in the data while keeping an uncertainty on the bubble  
1038 number density of about 5% (Shea et al., 2010). The analysis of 2,250 vesicles  
1039 on SEM images gave a bubble number density of  $4 \times 10^{14} \text{ m}^{-3}$  of melt and an  
1040 average vesicle radius of  $12.1 \mu\text{m}$ , similar to Plinian pumices from other erup-  
1041 tions (Figure B.1b, Klug et al., 2002; Adams et al., 2006; Rust and Cashman,  
1042 2011; Shea et al., 2012, 2014). The maximum bubble radius is about  $200 \mu\text{m}$   
1043 and bubbles within  $20\text{-}50 \mu\text{m}$  constitute the majority of the porosity (Figure  
1044 B.1). The bubble number density was assumed constant for all the GM pumices  
1045 and used in the percolation and bubble growth models.

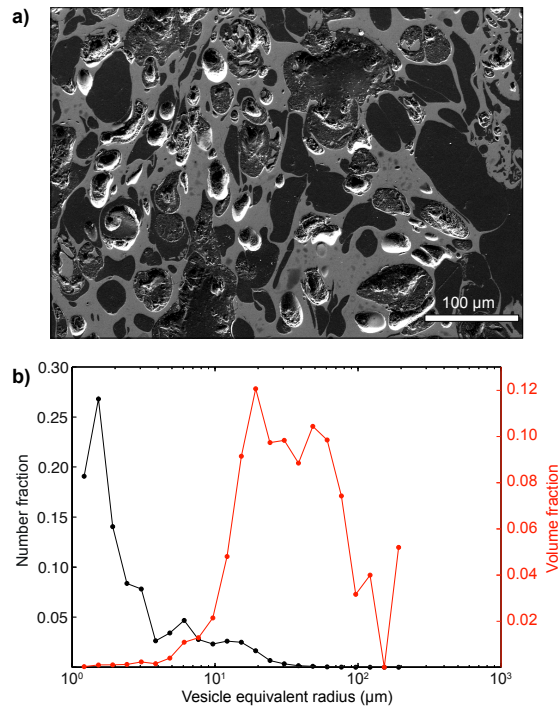


Figure B.1: (a) Backscattered scanning electron microscope image of a typical fallout Plinian pumice from the GM eruption. Vesicles appear in dark gray and the glass in light gray. (b) Vesicle number (black) and volume (red) fractions obtained by image analysis. Number density is dominated by vesicles with a radius  $< 5 \mu\text{m}$  while volume is dominated by vesicles 20-50  $\mu\text{m}$ . The average bubble radius is 12.1  $\mu\text{m}$ .

## 1046 **Appendix C. Percolation model**

1047 In our percolation model, spheres with different sizes are randomly placed  
1048 in a three-dimensional cubic-shaped volume of  $10^{-8}$  m<sup>3</sup>. Assuming spheres are  
1049 voids, the total porosity of the volume, its connected porosity, and its perme-  
1050 ability resulting from interconnections between spheres and the exterior of the  
1051 volume, are calculated. A list of spheres which size distribution conforms that  
1052 measured on the representative GM pumice (see Appendix B) is first gener-  
1053 ated. Three-dimensional coordinates locating the center of the spheres in the  
1054 cubic-shaped volume are then randomly generated. If the centers of two bubbles  
1055 of radii  $r_1$  and  $r_2$  are separated by a distance less than  $(1 - \epsilon/2) \times (r_1 + r_2)$ ,  
1056 where  $0 \leq \epsilon \leq 1$ , the two bubbles are considered connected (cf. Figure C.1  
1057 and paragraph below). The model then determines all the interconnections be-  
1058 tween the spheres and between clusters of spheres and the exterior of the volume  
1059 (permeable clusters), and reckons the connected porosity. The radius and fluid  
1060 conductance of the circular apertures connecting bubble pairs is calculated, and  
1061 the resultant permeability is then estimated based on an analogy with a network  
1062 of electrical conductors, where the pathway is treated as a network of discrete  
1063 resistances to fluid flow (Blower, 2001a,b).

1064 Figure C.1 illustrates the role of the geometrical parameter  $\epsilon$  in the perco-  
1065 lation model (Blower, 2001b). During magma ascent, growing bubbles impinge  
1066 upon one another and become deformed but may remain separated by a thin  
1067 film of glass (Figure C.1a), whereas spheres in the percolation model are usu-  
1068 ally considered connected as soon as they overlap. The parameter  $\epsilon$  is used  
1069 to account for the fact that two overlapping spheres in the percolation model  
1070 may not necessarily be considered connected (Figure C.1b-d; Blower, 2001b).  
1071 Everything else being equal, a higher value of  $\epsilon$  leads to less connected spheres,  
1072 a higher percolation threshold, and a lower permeability (Figure C.2).

1073 The number of spheres implemented in the model is adjusted so that the  
1074 total porosity and sphere number density of the volume are equal to those of  
1075 the pyroclast used to calculate the BSD (Appendix B). In order to investigate

1076 the relationships between  $\phi_t$ ,  $\phi_c$ , and  $k$ , numerous models with different  $\phi_t$  must  
 1077 be generated. This is achieved by multiplying by a factor 0.6 to 1.5 the radii of  
 1078 all the spheres and adjusting the number of spheres so that  $0.30 \leq \phi_t \leq 0.95$   
 1079 while the sphere (bubble) number density remains constant. Individual results  
 1080 obtained from the percolation model (i.e., different sets of  $\epsilon$ ,  $\phi_t$ ,  $\phi_c$ , and  $k$ ) were  
 1081 first fitted in order to obtain the connected porosity,  $\phi_c$ , only as a function of the  
 1082 total porosity,  $\phi_t$ . A least squares fit of all the model results obtained for each  
 1083  $\epsilon$  gives (Normalized Root Mean Square Error, NRMSE=0.83-0.97,  $n=3-50$ )

$$\phi_c = \phi_t + \beta \left( 1 - \frac{1}{\phi_t^\gamma} \right), \quad (\text{C.1})$$

1084 where  $1.5 \times 10^{-3} \leq \beta \leq 257 \times 10^{-3}$  and  $4.45 \leq \gamma \leq 6.89$  both depend on  
 1085 the value of  $\epsilon$  (Figure C.2a). Note that  $\phi_c$  is the percolating connected porosity  
 1086 here, that is the volume fraction of bubbles belonging to permeable clusters.  
 1087 The percolation threshold,  $\phi_{cr}$ , is obtained solely as a function of  $\epsilon$  (Figure  
 1088 C.2b, NRMSE=0.97,  $n=8$ ),

$$\phi_{cr} = 0.332 + 0.397\epsilon + 0.362\epsilon^2. \quad (\text{C.2})$$

1089 Note that  $\phi_{cr} \approx 0.3$  for  $\epsilon = 0$  (Equation (C.2), Figure C.2b), as in other studies  
 1090 (e.g., Feng et al., 1987; Sahimi, 1994; Blower, 2001b).

An empirical formulation for permeability as a function of  $\phi_t$  and  $\phi_{cr}$  is then  
 obtained by realizing a least squares fit to the permeability results (Figure C.2c,  
 NRMSE=0.84-0.96,  $n=3-50$ ),

$$k = b \times r^2 (\phi_t - \phi_{cr})^c, \quad (\text{C.3})$$

1091 where  $0.20 \leq b \leq 1.36$  and  $2.51 \leq c \leq 3.08$  depend on the value of  $\epsilon$ , and  
 1092  $r = [\phi_t / (N \times [1 - \phi_t]) \times 3/4/\pi]^{1/3}$ . Equation (C.3) is used in the bubble growth  
 1093 and conduit flow model with  $0.2 \leq \epsilon \leq 0.6$ .

1094 Calculation time of the percolation modeling increases exponentially with the  
 1095 number of spheres implemented. Therefore, spheres  $<10 \mu\text{m}$  were not modeled.  
 1096 This choice is justified by the fact that bubbles with a radius  $<10 \mu\text{m}$  represent

1097 a porosity of  $\approx 0.06$  while they account for about 90% of the bubble number  
1098 density of the pumice used to perform the BSD (Appendix B). Moreover, most  
1099 of the smallest bubbles are likely isolated (e.g., Klug et al., 2002; Giachetti et al.,  
1100 2010). If connected, their contribution to sample permeability is small because  
1101 permeability scales with the square of bubble radius (e.g., Saar and Manga,  
1102 1999; Blower, 2001a,b).

1103 The geometrical parameter  $\epsilon$  may be conceptually related to a capillary  
1104 number, scaling with melt viscosity. At least two capillary numbers can be  
1105 defined and that are related with the overall process of bubble impinging and  
1106 coalescence. First, growing bubbles in ascending magma impinge upon one  
1107 another and become deformed, but may remain separated by a thin film of  
1108 glass. The capillary number,  $Ca$ , associated with this deformation, which is the  
1109 ratio of shear stresses that deform the bubble to the surface tension stresses that  
1110 tend to keep the bubble spherical, depends linearly on viscosity (e.g. Rallison,  
1111 1984; Stone, 1994; Rust and Manga, 2002; Moitra et al., 2013). For  $Ca \ll$   
1112 1 bubbles will tend to remain spherical, while for  $Ca \gg 1$ , bubbles remain  
1113 deformed.  $Ca \approx 400$  for the GM magma at fragmentation (similar to estimated  
1114  $Ca \sim 10^2$ - $10^3$  for Vulcanian to ultraplinian eruptions at fragmentation, Moitra  
1115 et al., 2013), and vesicles in the GM pumices are mainly deformed (Figures  
1116 B.1a and C.1a). Second, for two bubbles to coalesce, the intervening melt film  
1117 has to drain to a thickness where it becomes unstable, ruptures, and forms a  
1118 hole (Klug and Cashman, 1996; Castro et al., 2012a; Nguyen et al., 2013), a  
1119 process speeded up by bubble growth. The capillary number associated with  
1120 film drainage is the balance, within the film, between capillary pressure causing  
1121 flow and viscous forces resisting flow. This capillary number also scales with  
1122 melt viscosity (e.g., Proussevitch et al., 1993b; Nguyen et al., 2013). Therefore,  
1123 everything else being the same, increasing melt viscosity leads to an increase in  
1124 the proportion of deformed bubbles, a slow down of the film thinning process, an  
1125 overall delay in bubble coalescence, and an increase of the percolation threshold.  
1126 Similarly, for relatively low  $\epsilon \lesssim 0.2$  in the percolation model, bubbles become  
1127 rapidly interconnected and  $\phi_{cr} \approx 0.3$ - $0.4$  (Figure C.2c), a percolation threshold

1128 observed for crystal-free Strombolian basaltic pyroclasts (Saar and Manga, 1999;  
 1129 Mueller et al., 2005) for which low Ca and rather round bubbles are expected  
 1130 (Moitra et al., 2013). For higher values of  $\epsilon$ , the percolation modeling predicts  
 1131 that  $\phi_{cr} \approx 0.45-0.70$ , consistent with higher values of  $\phi_{cr}$  suggested for more  
 1132 viscous silicic magma ( $> 0.5$ ; Eichelberger et al., 1986; Rust and Cashman,  
 1133 2011; Nguyen et al., 2014, Figure 2), for which much higher Ca are expected.

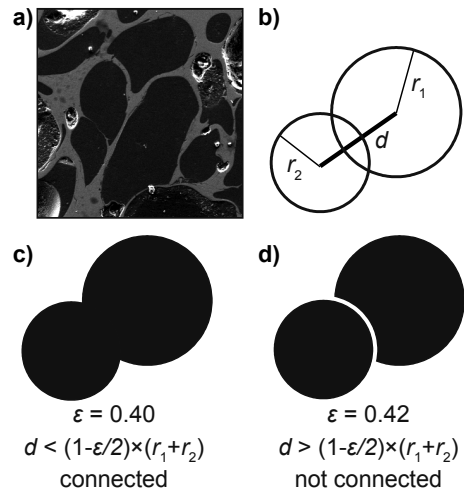


Figure C.1: Illustration of the geometrical parameter  $\epsilon$  used in the percolation model (Blower, 2001b). (a) SEM image of a GM pumice showing that vesicles can be deformed but remain separated by thin films of glass. (b) Two spheres of radii  $r_1$  and  $r_2$  randomly placed in the cubic-shaped volume overlap. (c) For  $\epsilon=0.40$ ,  $d < (1 - \epsilon/2) \times (r_1 + r_2)$ , and the two spheres are considered connected (or coalesced) and gas can flow between them. (d) For  $\epsilon=0.42$ ,  $d > (1 - \epsilon/2) \times (r_1 + r_2)$ , and the two overlapping spheres are considered isolated and gas cannot flow between them.

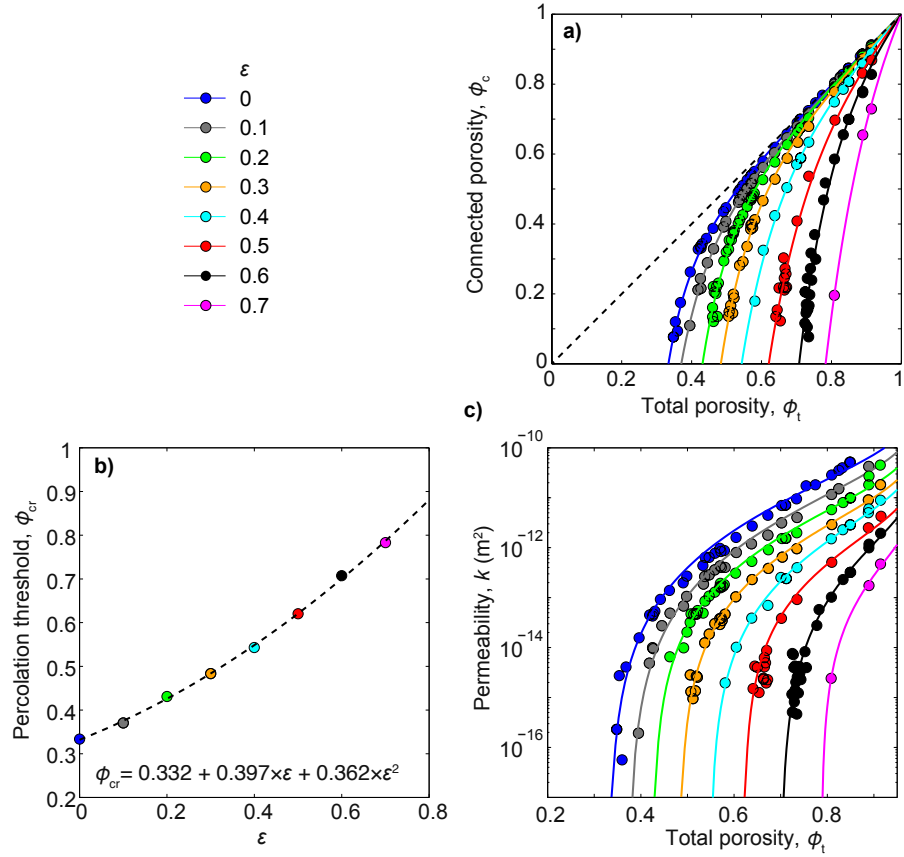


Figure C.2: Results from the percolation model (circles) for  $0 \leq \epsilon \leq 0.7$ . (a) Connected porosity,  $\phi_c$ , as a function of total porosity,  $\phi_t$ , and empirical fits (Equation (C.1)). (b)  $\phi_{cr}$  as a function of  $\phi_t$  and fit (Equation (C.2)). (c) Permeability,  $k$ , as a function of  $\phi_t$  and fits (Equation (C.3)). All fits are obtained using the least squares method.

## 1134 **Appendix D. Model sensitivity**

### 1135 *Appendix D.1. Sensitivity to initial pressure*

1136 Figures 3-5 show results that were obtained using an initial pressure of 100  
1137 MPa. Because Grove et al. (1997) estimated pre-eruptive pressure for the GM  
1138 magma between 100 MPa to 200 MPa, we compared model results for three  
1139 initial pressures: 100 MPa, 150 MPa and 200 MPa, corresponding to initial  
1140 water contents of 3.9 wt%, 5.0 wt% and 5.9 wt%, as well as initial depths of  
1141 3.9 km, 5.9 km and 7.8 km. Figure D.3 shows that  $Pe_\eta$  at which  $\chi$  reaches a  
1142 minimum increases with increasing initial pressure. At a given  $Pe_\eta$  the value of  
1143  $\phi_t$  at which rapid pressure buildup occurs increases with initial pressure, and  
1144 fragmentation is expected to occur at shallower depths. Correspondingly, the  
1145 decompression rate at fragmentation also increases with initial pressure, as does  
1146 the dissolved water content, whereas melt viscosity decreases.

### 1147 *Appendix D.2. Sensitivity to bubble number density, $N$*

1148 We compare the results of models performed using different bubble number  
1149 densities,  $N$ , all else being the same ( $Q = 1.1 \times 10^7 \text{ kg.s}^{-1}$ ,  $a = 24.2 \text{ m}$ , initial gas  
1150 pressure of 100 MPa,  $\epsilon = 0.2$ ). Figure D.1 shows that if the original  $N = 4 \times 10^{14}$   
1151  $\text{m}^{-3}$  shown with blue curves is increased (decreased) by a factor 2, the predicted  
1152 fragmentation depth is decreased (increased) by about 9 m (22 m). Moreover, for  
1153 lower  $N$ , fragmentation occurs at higher overpressure, velocity, decompression  
1154 rate and bubble radius, while the melt viscosity remains relatively constant.  
1155 If  $N$  is decreased by an order of magnitude ( $N = 4 \times 10^{13} \text{ m}^{-3}$ , red dotted  
1156 curve), then the magma runs out of pressure before bubble overpressure reaches  
1157  $\Delta P_f$ . Note that the error associated with the method used to calculate  $N$  is  
1158 expected to be less than 5% (Appendix B Shea et al., 2010) and we do not  
1159 expect variations of  $N$  within the whole sample suite to exceed a factor 2.

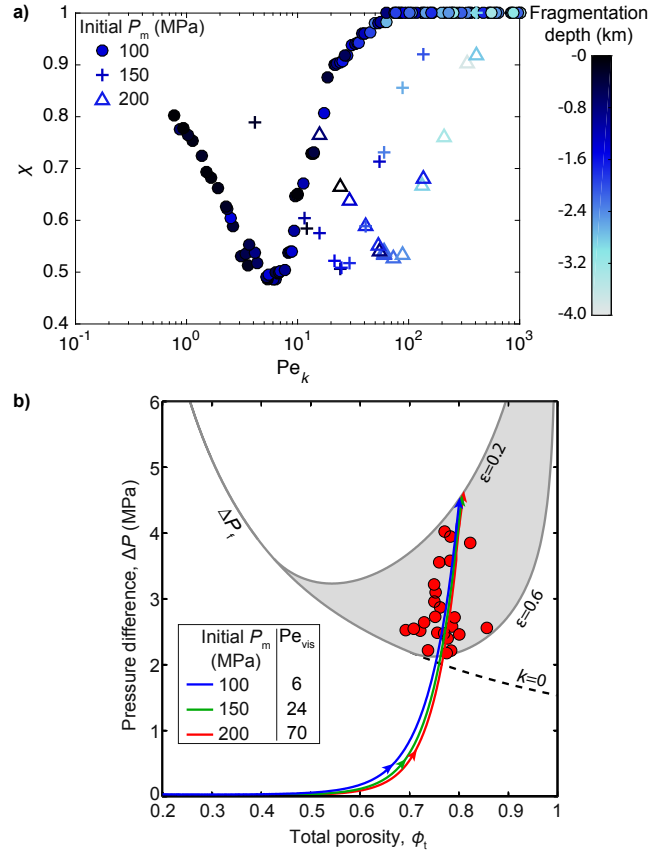


Figure D.3: Sensitivity of the results to the value of the initial pressure. **(a)**  $\chi$  as a function of  $Pe_\eta$  for initial  $P_g = 100, 150,$  and  $200$  MPa. Minimum  $\chi$  is obtained for  $Pe_\eta \approx 6, 24,$  and  $70,$  respectively. **(b)** Predicted bubble overpressure as a function of total porosity for one of the best case scenarios for each initial pressure.

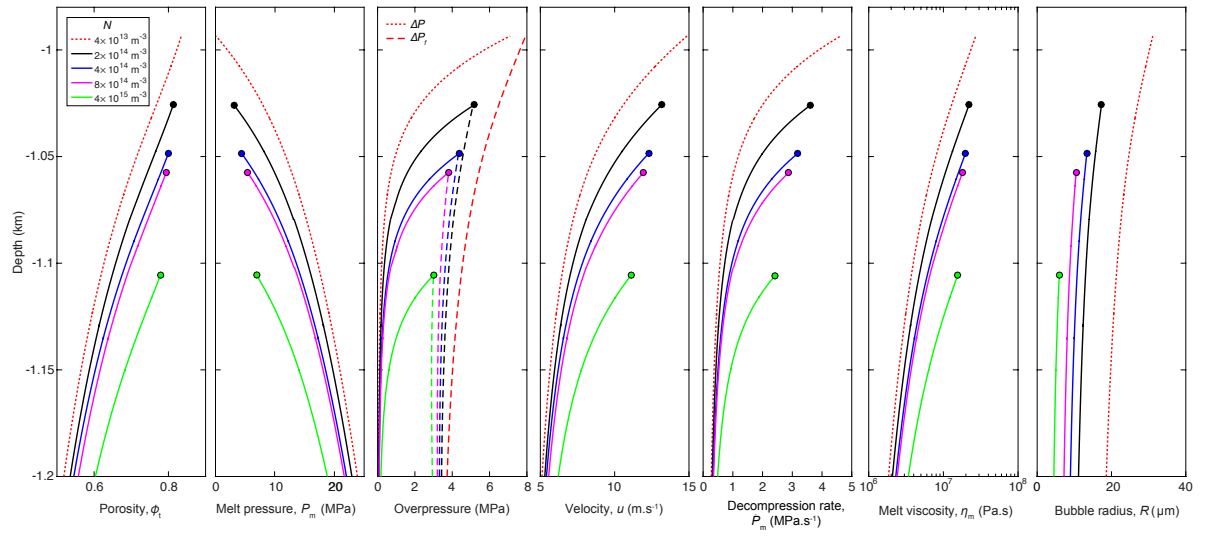


Figure D.1: Results for different values of  $N$ , everything else being the same. Expected fragmentation is symbolized by a solid circle. For  $N = 4 \times 10^{13} \text{ m}^{-3}$  (red curve), the ambient pressure reaches 0.1 MPa before the magma is expected to fragment.

1160 *Appendix D.3. Sensitivity to initial bubble radius*

1161 We compare the results of models performed using different initial bubble  
 1162 radii ( $10^{-8}$ ,  $10^{-7}$ , and  $10^{-6}$  m), all else being the same ( $Q = 1.1 \times 10^7$  kg.s $^{-1}$ ,  
 1163  $a = 24.2$  m, initial gas pressure of 100 MPa,  $\epsilon = 0.2$ ). Figure D.2 shows  
 1164 that the results are not modified in any significant way by variations of the  
 1165 initial bubble radius by an order of magnitude. Magma properties at expected  
 1166 fragmentation remain identical from one case to another, only the expected  
 depth of fragmentation varies by several meters.

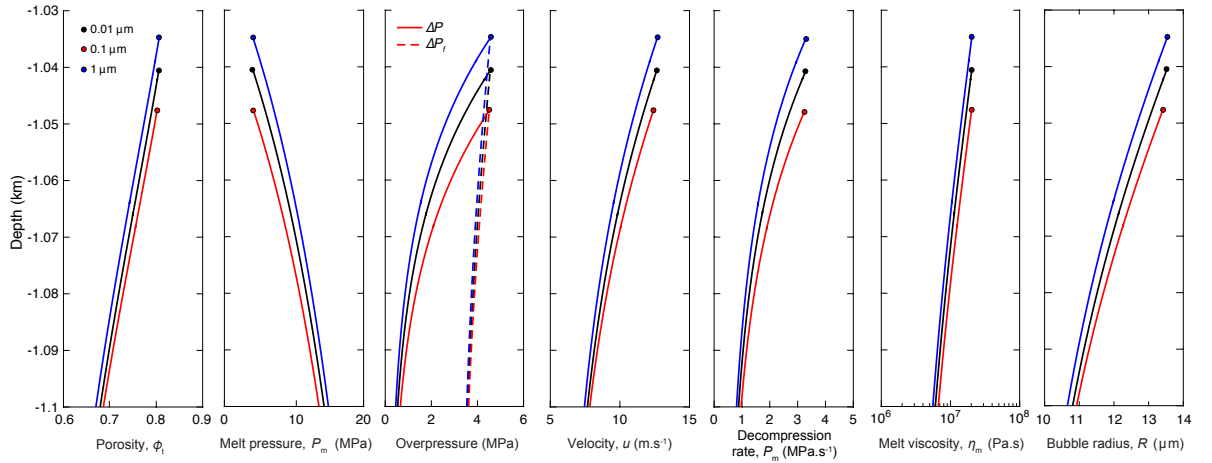


Figure D.2: Results for different values of initial bubble radius, everything else being the same. Expected fragmentation is symbolized by a solid circle. Only the expected depth of fragmentation varies from one initial bubble radius to another.

1167

1168 **Appendix E. Darcian and non-Darcian permeabilities**

1169 The inertial permeability of the sub-samples (1-9 sub-samples per sample,  
 1170 see Section 3.1),  $k_2$ , was obtained as indicated in Appendix A. The inertial  
 1171 permeability shows a power-law relationship with the Darcian permeability,  $k$ ,  
 1172 as illustrated in Figure E.1 (linear trend on a log-log graph). The power-law  
 1173 relationship,  $k_2 = 10^{7.68} \times k^{1.312}$ , was determined using a least-squares fit to the  
 data (NRMSE=0.91,  $n=76$ ).

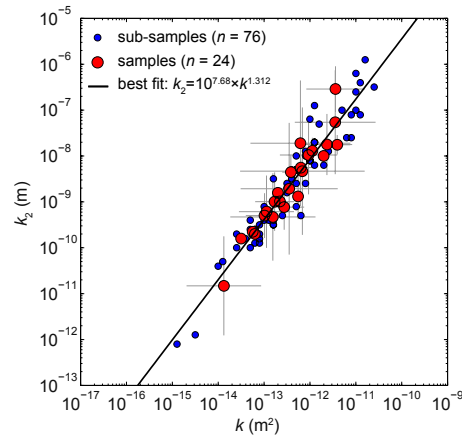


Figure E.1: Inertial permeability,  $k_2$ , as a function of Darcian permeability,  $k$ , for 76 sub-samples from a total of 24 GM pumice samples. The solid black line corresponds to  $k_2 = 10^{7.68} \times k^{1.312}$ , the best fit in a least squares sense.

1174